THE OPTICAL PROPERTIES, OXIDATION BEHAVIOR AND THERMAL STABILITY OF BLACK CHROME SELECTIVE SOLAR ABSORBERS

By

KARTIK SHANKER

A DISSERTATION PRESENTED TO THE GRADUATE SCHOOL
OF THE UNIVERSITY OF FLORIDA IN PARTIAL FULFILLMENT
OF THE REQUIREMENTS FOR THE DEGREE OF DOCTOR OF PHILOSOPHY

UNIVERSITY OF FLORIDA

1983

ACKNOWLEDGEMENTS

The author thanks all the members of his supervisory committee for their encouragement and assistance. In particular, he appreciates the patient guidance and constant encouragement of his advisor, Dr Paul H Holloway. He would also like to thank Susan K Hofmeister for assisting with Auger electron spectroscopy studies and his wife, Latha, for her help with computer-related analysis. Last, but not least, the author appreciates the excellent typing of this manuscript by Debbie Perrine

Acknowledgements are also due to Sandia National Laboratories, Albuquerque, NM, and the U.S. Department of Energy through the Solar Energy Research Institute for research support under grant #DE-FG02-79ER10541

TABLE OF CONTENTS

Page

ACKNOWLEDGEMENTS ii

ABSTRACT vi

CHAPTER

I PHOTOTHERMAL SOLAR ENERGY CONVERSION 1
- Introduction 1
- Spectral Selectivity 4
- Black Chrome Selective Solar Absorbers 5
- Microstructure of Black Chrome Films 11
- Optical Properties 13
  - Solar Absorptance 14
  - Thermal Emittance 14

II THEORY 16
- Introduction 16
- Maxwell-Garnett Theory 17
- Reflectivity Curves 24
- Model Calculations 26
  - Model A 26
  - Model B 33
- Reflectance Calculations 39
- Uncertainties in Model Calculations 47
  - Differential Sputtering Effects 47
  - Effect of Surface Roughness 47
  - Effect of Voids and Agglomerate Size 48
  - Uncertainty in the Refractive Index 50
- Effect of Structure on Thermal Emittance 51
- Conclusions 52

III ELECTRODEPOSITION 55
- Introduction 55
- Experimental Procedure 56
- Experimental Variables 60
- Sequence of Experiments 61
- Results 63

CHAPTER Page

IV OPTICAL PROPERTIES 65

Introduction 65

Measurement of Solar Absorptance 65

Measurement of Thermal Emittance 73

Results 74
  Reflectance Measurements 91
  Solar Absorptance 98
  Emissivity Measurements 100

Discussion 100

V ANALYSIS OF BLACK CHROME FILMS 102

Introduction 102

Experimental Procedure 102

Results 103
  XPS Results 104
  AES Results 107
  Thermal Desorption Results 122
  Effect of Oxide Content on Optical Properties 132

Summary of Results 135

VI OXIDATION OF PURE CHROMIUM 137

Introduction 137

Experimental Procedure 138

Results 139

Discussion 144

VII DISCUSSION OF EXPERIMENTAL RESULTS 156

Data Reduction 156

Effect of Oxide Content on Optical Properties 162
  Solar Absorptance 162
  Thermal Emittance 165
  Prediction of Microstructure from Optical Properties 165

Oxidation Behavior of Black Chrome 166

Effect of Minor Constituents in the Film 172

Comparison with Model Calculations 176

CHAPTER Page

VII DISCUSSION OF EXPERIMENTAL RESULTS (continued)
Effect of Deposition Conditions 178
Appearance of Black Chrome Films 178
Chromic and Acetic Acid Concentration 180
Fe^{+3} Concentration 180
Cr^{+3} Concentration 182
Current Density and Deposition Time 184
Optimum Deposition Conditions 184

VIII CONCLUSIONS 188

APPENDIX

A BRUGGEMAN SYMMETRICAL EFFECTIVE MEDIUM (BEM) THEORY 188

B PROCEDURE FOR DEPOSITION OF BLACK CHROME FILMS ONTO NICKEL PLATED PLAIN CARBON STEEL SUBSTRATE 192

C ANALYSIS OF THE ELECTRODEPOSITION BATH 194
Cr^{+3} Concentration 194
Analysis of CrO_3, Acetic Acid and Fe^{+3} Concentration 196

D QUANTIFICATION OF AUGER SPUTTER DATA 200

E EFFECT OF SiO_2 OVERLAYER ON BLACK CHROME OXIDATION 203

REFERENCES 207

BIOGRAPHICAL SKETCH 215

Abstract of Dissertation Presented to the Graduate School
of the University of Florida in Partial Fulfillment of the
Requirements for the Degree of Doctor of Philosophy

THE OPTICAL PROPERTIES, OXIDATION BEHAVIOR AND THERMAL STABILITY OF BLACK CHROME SELECTIVE SOLAR ABSORBERS

By

Kartik Shanker

December, 1983

Chairman Paul H Holloway
Major Department Department of Materials Science and Engineering

Photothermal solar energy converters presently offer the highest conversion efficiencies for medium power generation Since they must operate at temperatures > 300°C, spectral selectivity is required to minimize thermal re-radiation losses Electrodeposited black chrome absorbers are a promising candidate for use in such systems even though the present generation shows rapid degradation at temperatures > 300°C

The oxide content of these films was determined by Auger electron spectroscopy Sputter reduction of Cr_2O_3 to Cr was observed, but remained constant after ~ 1 minute of sputtering (< 50 Å) Differential sputtering of Cr_2O_3 relative to Cr was also observed However, both sputtering effects were small

Black chrome films contain metallic chromium, chromium oxide and voids Under the optimum deposition conditions, these films maintained their solar absorptance relatively constant at its highest value during thermal exposure This was because the films maintained their oxide

content in the range of 40 ~ 75% (± 5%) oxide during thermal exposure. Above and below this range, the solar absorptance decreased rapidly. In this range, the thermal emittance decreased linearly with increasing oxide content.

Both black chrome films and chromium show logarithmic oxidation behavior during thermal exposure. Rapid initial oxidation was followed by increasingly slower oxidation. Thus, the as-deposited oxide did not protect the chromium particles from further oxidation and the oxide that forms during thermal exposure is required for passivation. The thickness of the passivating layer is a function of temperature and time and results in a smaller size of Cr particulate. In addition, experimental evidence suggests that oxidation during thermal exposure results in an outer Cr_2O_3 layer which thickens at higher temperatures or longer times and results in a smaller increase in the oxide content deep in the film. Therefore, void volume and void distribution, even if initially uniform, become non-uniform on thermal exposure.

The Maxwell-Garnett theory can be extended to predict the behavior of black chrome films with respect to changes in their dielectric constant, reflectance, absorptance and emittance. The microstructural model, comprised of a sphere of chromium covered with a dense oxide and embedded in a medium of as-deposited oxide and air, gives reasonable correlations with observed values, but is limited by the non-incorporation of changes in voids and agglomerate sizes.

CHAPTER I
PHOTOTHERMAL SOLAR ENERGY CONVERSION

Introduction

Solar energy is being increasingly viewed as a viable source of usable energy. In addition, it has the advantages of being environmentally benign and inexhaustible in quantity.[1,2] The AM0 and AM2 solar energy spectra are shown in Figure 1; AM0, called air mass zero, refers to the spectrum in outer space, while AM2, called air mass two, refers to the spectrum after it has passed through two air masses. Note that 98% of the AM2 energy is at wavelengths shorter than 2 um. For comparison, the spectral selectivity of the human eye is also shown; it covers only about 40% of the AM2 radiation. The interactions between the air masses and solar radiation results in both a decrease in the total amount of radiated energy and an increase in the diffuse component. The AM0 solar radiation has about 1360 watts/m^2, while the AM2 radiation has only about 755 watts/m^2.[3]

A wide range of technologies is necessary to accomplish the goal of converting solar energy into useful forms of energy such as heat, chemical fuels or electricity. The extent to which solar energy is presently being utilized is, however, primarily restricted by the technological limitations restricting their economical usage.[2] Nowhere is this more obvious than in the materials used for conversion. The converter materials in the present generation have low conversion efficiencies, short lifetime and/or high cost.[1-4] Thus, for solar energy to become a practical source of energy, improvements in the converter material are of paramount importance.

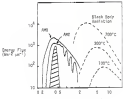

Figure 1.1 Spectral distribution of solar radiation at AM0 and AM2 and black body re-radiant spectra. The hatched portion represents the spectral sensitivity of the human eye.

Direct solar energy conversion can be classified as photoelectric, photochemical or photothermal, depending on the product of conversion. Photochemical and photothermal conversions presently constitute the largest segment. However, photochemical conversion is not yet directly available as chemical energy for industrial purposes,[2] it is almost exclusively being used by nature, e.g., plants. The two classes of practical interest are photoelectric and photothermal. The present generation of photoelectric converters have low efficiencies ($\leq$ 18%) and are expensive.[2-5] Photothermal converters, in contrast, often show efficiencies of 50% or more, thereby providing incentive to improve their lifetime and reduce their cost. This directly results in the present research, viz., investigation of the factors that control the properties and stability of one of the more promising photothermal converters, the black chrome selective solar absorber coatings.

Photothermal solar energy conversion is of interest since it shows promise for utilization not only as thermal energy, but also as a viable route for electrical power generation.[3] In photothermal conversion, photons of solar radiation are converted to phonons in the absorbing material. The energy can then be transferred to a working fluid, such as steam, which provides the necessary energy (through a thermodynamic cycle) for an electrical generator.[2,6]

A solar collection system typically consists of an absorbing surface, glazing to reduce convective heat loss, insulation and a heat transfer medium.[3,7] For systems designed for higher temperature (and energy), reflectors are used to concentrate the radiation. For concentrations greater than tenfold, tracking of the sun is essential.[1,3]

A large number of potential candidates exist for use as photothermal converters [1-12] These range from an absorber as simple as black paint to something as complex as a multilayer stack or a wavelength discriminating surface [1,12] For low temperature applications (≲ 200°C), the number of suitable candidates is large Economy then becomes the primary reason for choosing a particular type of absorber At temperatures above 250°C, the number of suitable materials is sharply reduced since most absorbers degrade very rapidly at these temperatures [8,13] Such high temperatures are, however, required if photothermal conversion is to prove viable for electrical power generation

Spectral Selectivity

Apart from resistance to degradation, photothermal converters must have spectral selectivity for minimal losses [1] This is particularly important for high temperature (≥ 250°C) concentrating collectors The reason for this can be understood from Figure 1.1, which not only shows the solar energy spectra, but also the radiation spectrum of a black body as a function of temperature High conversion efficiencies can only be achieved if the body absorbs as much of the solar radiation as possible and prevents much of the black body re-radiation in the infrared region Comparing the solar AM2 spectrum and that for a black body at 700°C in Figure 1.1, there is an overlap of two spectra of only about 5% on either side of 2 μm This is because the solar energy spectrum has ~ 95% of its energy at wavelengths less than 2 μm, while the re-radiant black body spectrum has ~ 95% of its energy at wavelengths greater than 2 μm Therefore, an absorber system that has high absorptance at wavelengths less than 2 μm with simultaneous suppression of emission above 2 μm would have the highest possible converter efficiency. The spectral profile of an ideal converter is shown in Figure 1.2.[1] A typical real converter profile is also included. It is important to note that such spectral selectivity is important only when working at higher temperatures, i.e., at temperatures above 250°C. At lower temperatures, the decrease in efficiency due to nonselectivity is quite small. Such systems rarely require the use of spectrally selective absorbers. Note, however, that a small advantage accrues to these absorbers if the cost is the same as a nonselective absorbers.[1]

The earliest practical use of spectral selectivity in energy conversion was reported by Tabor[1,14,15] and Gier and Dunckle[1,16] in 1955. Although the simplest spectrally selective absorber would be a single absorber layer, no such material is known to exist in nature.[1] Furthermore, if such a material had existed, it would have been at a higher temperature than its surroundings. As a result, its decomposition would probably have been rapid. Some materials do exist, however, that have their optical properties close to the desired spectral profile. The reflectance of two such materials is plotted in Figure 1.3. Note that for opague materials, high reflectance implies low absorptance and vice versa. Metals typically show high reflectance except at very low wavelengths, while a heavily doped semiconductor shows high reflectance only in the very far infrared region. To shift the spectral profile of either material is difficult and the practicality of doing so questionable.[1]

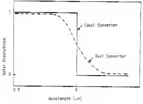

Figure 1 2 Solar absorptance profile of ideal and real solar energy absorbers

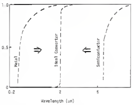

Figure 1.3 Spectral profiles of an ideal converter versus that of a heavily doped semiconductor and a typical metal (ref. 1)

Another approach used to generate the desired spectral profile is by the use of wavelength discrimination. Here, by making suitable changes in the surface, e.g., by creating an intentionally roughened surface, spectral selectivity can be attained. The surface character prevents the re-radiation without significantly reducing absorption.[1,17,18] However, structural surface effects are difficult to characterize and also difficult to generate on a practical scale.

The next level of complexity involves the use of two materials in tandem to achieve the desired spectral profile. At least two configurations are possible, as shown in Figure 1.4. Of the two, the dark mirror configuration has been more actively investigated. One likely reason is because metals form a very attractive group of white reflectors. They also have excellent thermal conductivity. Their high reflectance in the thermal infrared effectively suppresses the emittance while their high thermal conductivity results in rapid transfer to the working fluid. Thus, almost without exception, the dark mirror spectrally selective absorber systems have a white metal reflector on which is deposited the absorber coating.

Black Chrome Selective Solar Absorbers

A large number of possible candidates have been investigated (and suggested) as the absorber coating.[3-13,19-24] Amongst these the black metals (particularly black nickel, black copper and black chromium) have received the most attention.[12] An important reason is because they can be coated by electrodeposition techniques (or by other relatively inexpensive techniques, such as spraying).[3,12,25] This makes them economically

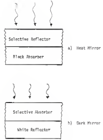

Figure 1.4 Two possible absorber-reflector tandem combination solar absorbers.

more attractive than other coatings, such as molybdenum-based coatings that require more expensive vacuum deposition methods.[1,3,12,24] Amongst the black metals, black chromium (henceforth called black chrome) coatings are being investigated most widely for medium temperature applications. This is because both the black copper and black nickel coatings are unstable above 300°C.[12,26-28] Black chrome coatings have shown long term stability at temperatures of ~ 400°C when plated under certain conditions.[13,29] Although black chrome has been investigated a number of times,[15,30,31] the characterization of its structure and its correlation with optical properties is far from complete. Furthermore, understanding of the factors that control their long term stability is also incomplete.

The first mention of black chrome as a prospective solar absorber coating was made by Tabor in 1959.[15,32] But it was not until 1974 that detailed stuides were reported on coatings deposited using a proprietary bath developed by the Harshaw Chemical Company.[33,34] Since then, numerous studies have been reported where the feasibility of using the electrodeposited black chrome films for mid-temperature solar absorbers was investigated.[8,11-15,20,25,30,32,35] The majority of these coatings had been electrodeposited using the Chromonyx bath developed by Harshaw.[36] Irrespective of the conditions under which the films have been deposited, all the investigators report a mixture of chromium and chromium oxide(s) in the film. Pettit and Sowell,[30,32] Braun et al.,[37] and Fan and Spura[38] all present evidence that the outer layer of these films is oxide rich and becomes more metallic as the substrate is reached, this agrees with the results discussed in this dissertation. Clark et al.[39] claim that the oxygen and chromium are uniformly distributed, while Zajac et al [40,41] suggest the presence of hydrated oxide in the films.

Evidence, reported in this dissertation and available from a number of sources,[30,32,35] suggests a strong correlation between the deposition conditions and the properties of the film. For example, reducing the Cr^{+3} concentration from 16 g/l to 6 g/l in the plating bath appears to have a significant effect on the long term stability of these films.[31,35]

Microstructure of Black Chrome Films

Black chrome films are a composite of chromium metal, chromium oxides and possibly other compounds, such as chromium hydroxides. The films are not very dense. Sweet and Pettit[32] have estimated the void fraction to be $\gtrsim 0.6$. The optical properties of black chrome films depend on the relative amounts of each of the constituents and the form (size, shape and distribution) in which they are present.[32]

There have been several studies of the microstructure of the coatings.[31,32,37,38,42] All suggest that the films contain small metallic chromium particles embedded in chromium oxide. One suggested model is shown in Figure 1.5. The metallic particles are envisaged as being embedded in chromium oxide agglomerates which, in turn, are separated from one another by voids. The metallic chromium particle size has been estimated to range from 0.02 ~ 0.1 μm in diameter, while the oxide agglomerate size ranges up to ~ 0.2 μm. Since the nature of the interaction depends on the microstructure of the film, the optical properties are directly related to the structure of the film.

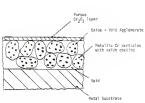

Figure 1 5 Suggested model of the microstructure of black chrome selective solar absorber films (derived from ref. 32)

Although progress had been made in establishing correlations between optical properties, film structure and the deposition conditions,[33] much more work was needed to satisfactorily explain the interdependence of the structure of these black chrome films, their deposition conditions, optical properties and long term stability at elevated temperatures This research attempts to extend the degree of understanding regarding black metal and particularly black chrome selective solar absorber films. The results (presented in the following chapters) show that the deposition conditions control the optical properties and their thermal stability. The as-deposited oxide only weakly passivates the metallic Cr particles. Thus, a passive oxide layer forms rapidly on thermal exposure, its thickness being a function of temperature and time Since the optical properties remain at their optimum when the oxide is maintained between ~ 40 and 75 vol.%, deposition conditions that cause the as-deposited film to have ~ 30% oxide create relatively stable films The rapid formation of the passive oxide layer on thermal exposure raises the oxide content into the optimum range

Optical Properties

The two optical properties of interest are the solar absorptance (α_s) and the thermal emittance (ε) These reflect the ability of the absorber system to both absorb the incident solar energy and minimize the re-radiation losses, respectively. Therefore, a good solar absorber system must have high solar absorptance coupled with low thermal emittance.

Solar Absorptance (α_s)

The expression for the wavelength-dependent solar absorptance is given by[1,12]

$$\alpha_\lambda(\mu,\phi) = \frac{J_{\lambda,a}(\mu,\phi)}{J_{\lambda,i}(\mu,\phi)} \tag{1.1}$$

where a and i are subscripts used for absorbed and incident radiation, respectively, μ is the cosine of the polar angle and ϕ is the azimuthal angle that is absorbed by plane surface, $J_\lambda(\mu,\phi)$ refers to the spectral irradiance of the radiation.

The hemispherical solar absorptance, α_s, is calculated by integration over the entire wavelength and hemispherical angle ranges. This results in

$$\alpha_s = \frac{\int_0^\infty \int_0^{2\pi} \int_0^1 \alpha_\lambda(\mu,\phi) J_{\lambda,i}(\mu,\phi)\mu d\mu d\phi d\lambda}{\int_0^\infty \int_0^{2\pi} \int_0^1 J_{\lambda,i}(\mu,\phi)\mu d\mu d\phi d\lambda} \tag{1.2}$$

In actual usage, the calculation is greatly simplified, as explained in Chapter IV.

Thermal Emittance (ε)

The thermal emittance represents the fraction of the radiant energy emitted by the surface in comparison to that emitted by a perfect black body at the same temperature, i.e.,[1,12]

$$\varepsilon = \frac{\int_0^\infty \varepsilon(\lambda)\ e_{BB}(\lambda,T)d\lambda}{\int_0^\infty e_{BB}(\lambda,T)d\lambda} \tag{1.3}$$

where

$$\varepsilon(\lambda) = \frac{J_{\lambda}\ (\mu,\phi)}{J_{b,\lambda}(\mu,\phi)} ,$$

the subscript b refers to the radiancy of a black body, and

$\varepsilon_{BB}(\lambda,T)$ = thermal emittance of a black body at wavelength and temperature T.

Measurement of thermal emittance is also quite straightforward The practical method used is explained in Chapter IV.

CHAPTER II
THEORY

Introduction

Black chrome films are a composite of chromium metal, chromium oxides and possibly other compounds, such as chromium hydroxides The materials are not very dense Sweet and Pettit[32] have estimated the void volume fraction to be $\gtrsim 0.6$ Thus, in order to calculate the complex dielectric constant of the film, the individual constituents, their dielectric constants, volume, size and shape must be known Furthermore, other relevant factors, such as distribution and orientation of the particles, must be known. It is, therefore, evident that calculation of the optical properties is complicated by the need to know the values and the effect of such a large number of variables

The general theory of dielectric constants and the conductivities of inhomogeneous media has been reviewed by Landauer [43] Siever[18] has discussed their application to spectral selectivity, but with major emphasis on composites having particles much smaller than the wavelengths of interest ($\lesssim$ 100 Å in diameter) The results are not easily extendable to composites having larger sized particles, which is the case for black chrome electrodeposited films (see following chapters)[32]

Although the theory of Mie[44] and Debye, as cited in Kerker,[45] offer a complete description for the special case of a homogeneous sphere in a homogeneous medium (providing the frequency dependence of the refractive index is known), the general problem of the electromagnetic response of an isolated conductor of arbitrary size, shape and frequency-dependent dielectric constant has not been solved

There are two major theories used to calculate inhomogeneous media dielectric constants. These are the Maxwell-Garnett and the Bruggeman symmetrical effective medium[46-49] theories. The Maxwell-Garnett theory (henceforth called MG theory) is explained in the following section while the Bruggeman effective medium theory (henceforth called BEM theory) is explained in Appendix A. Although several papers have compared calculated values of the complex dielectric constant with experimental results for black chrome films,[32,50-57] there is still no unifying model for such films. One important reason is the large number of parameters involved, which makes the number of possible calculations very large

Maxwell-Garnett Theory (MG)

This is one of the major theories used to calculate the dielectric constants of composite films.[46,47] Although the theory goes under the name "Maxwell-Garnett," it is derived from the Clausius-Mossotti relation.[43,58-60] Garnett's derivation is based on Maxwell's equations for propagating waves, not just on static behavior, thus the name "Maxwell-Garnett." The major assumption used to derive the dielectric constant ε_{MG} with the MG theory is that the composite medium is composed of isolated inclusions of one or more materials in a continuous matrix material. By isolated, it is meant that the perturbation in the fields within the matrix due to one inclusion does not extend to any of the other inclusions.

Consider the case of spherically symmetric polarizable entities immersed in vacuum ($\varepsilon=1$). If there are n spheres per unit volume, the polarization, $\bar{P}$, of the medium will be

$$\overline{P} = n\overline{p} \tag{2.1}$$

where $\overline{p}$ is the (average) polarization of each spherical particle

Due to the effect of polarization, the field will be a combination of the regular electromagnetic field, $\overline{E}_0$, and the polarization, i.e.,

$$\overline{E} = \overline{E}_0 + 4\pi\overline{P} = \overline{E}_0 - 4\pi n\overline{p} \tag{2.2}$$

Equation (2.2) is evaluated by assuming that the field $\overline{E}_0$ is unaffected by the presence of the dipole field. Out of the total field of $-4\pi n\overline{p}$, one third arises from inside the polarized volume, the remaining two thirds thus arises from outside this volume.[43,46] This result is obtained assuming spherical symmetry, but without assuming a uniformly polarizable sphere. Thus, the effective field is (from equation (2.2))

$$\overline{E}_{eff} = \overline{E}_0 - \frac{2}{3} \cdot 4\pi\overline{p} = (\overline{E} + 4\pi\overline{p}) - \frac{8}{3}\pi\overline{p}$$

or

$$\overline{E}_{eff} = \overline{E} + \frac{4}{3}\pi\overline{p} \tag{2.3}$$

Equation (2.3), also called the Lorentz expression, is valid only for small particles in a medium that has no dimension as small as the wavelength of light.[46] This provision is satisfied, except for thin films. Assume

$$\overline{p} = \alpha\overline{E}_{eff} \tag{2.4}$$

where α = polarizability, then in the effective medium theory,

$$(\varepsilon-1)\overline{E} - 4\pi n\overline{p} = 4\pi n\alpha\overline{E}_{eff} = 4\pi n\,(\overline{E}+\tfrac{4}{3}\pi\overline{p})$$

$$(\varepsilon-1)\overline{E} = 4\pi n\,(\tfrac{\varepsilon+2}{3})\overline{E}$$

or

$$\frac{(\varepsilon-1)}{(\varepsilon+2)} = \frac{4\pi n}{3} \tag{2.5}$$

Assuming that the polarizable entity is a sphere of dielectric constant ε_1 and radius r, then[43]

$$\alpha = \frac{(\varepsilon_1-1)}{(\varepsilon_1+2)} r^3 \tag{2.6}$$

Combining (2.5) and (2.6),

$$\frac{\varepsilon-1}{\varepsilon+2} = \eta \frac{\varepsilon_1-1}{\varepsilon_1+2} \tag{2.7}$$

where η = fraction of space occupied by material 1. If the surrounding medium is a material of dielectric constant ε_0 (instead of vacuum), equation (2.7) becomes

$$\frac{\varepsilon-\varepsilon_0}{\varepsilon+2\varepsilon_0} = \eta_1 \frac{\varepsilon_1-\varepsilon_0}{\varepsilon_1+2\varepsilon_0} \tag{2.8}$$

Generalizing

$$\frac{\varepsilon-\varepsilon_0}{\varepsilon+2\varepsilon_0} = \sum_i \eta_i \frac{\varepsilon_i-\varepsilon_0}{\varepsilon_i+2\varepsilon_0} \tag{2.9}$$

where the summation is over all the particles within a dielectric of constant properties. This result has been written by Böttcher[61] as follows

$$\frac{\varepsilon-1}{\varepsilon+2} = \frac{4\pi}{3} \sum_k N_k \alpha_k \tag{2.10}$$

where

N_k = number density of the kth particle

α_k = polarizability of the kth particle

The generalized equations, (2.9) and (2.10), are not as well founded as (2.8) since they assume that the same effective field, $\overline{E} + \frac{4\pi}{3}\overline{p}$, acts on all the polarizable entities. This is not very realistic since, on the average, a greater polarization surrounds a highly polarizable entity than a poorly polarizable one.[43] One other important feature to be observed from equations (2.7) to (2.10) is that the results obtained will be different depending on whether the system is viewed as species 1 embedded in species 2 or vice versa. This feature has been discussed in detail by Landauer.[43]

Several approaches have been used to obtain ε_{MG} for the system where the inclusions are ellipsoids rather than spheres.[32,43,62] Assuming that the ellipsoids are aligned with each other and embedded in an isotropic medium, Cohen et al.[43,62] have proposed a form of equation (2.8) in MKS units as

$$\frac{\varepsilon-\varepsilon_0}{L_m\varepsilon+(1-L_m)\varepsilon_0} = \delta\,\frac{\varepsilon_1-\varepsilon_0}{L_m\varepsilon_1+(1-L_m)\varepsilon_0} \tag{2.11}$$

where $L_m = \frac{n_m}{4\pi}$, δ is the Kronecker delta and n_m is the depolarization factor for the axis under consideration. Equation (2.11) is different from that proposed by Galeener[63] and Granqvist,[64] which is (in MKS units)

$$\frac{\varepsilon-\varepsilon_0}{\varepsilon+2\varepsilon_0} = \frac{1}{3}\,\delta\,\frac{\varepsilon_1-\varepsilon_0}{L_m\varepsilon_1+(1-L_m)\varepsilon_0} \tag{2.12}$$

Cohen et al.,[43,62] who proposed equation (2.11) have objected to equation (2.12) because its Lorentz sphere derivation gives unreasonable results if the entities are flat disks perpendicular to the field, these are discussed in more detail elsewhere.[43,62] The derivation of equation (2.11) assumes that the Lorentz cavity[65] has the same shape as the particles (i.e., ellipsoidal). Intuitive arguments suggest that the same depolarization factor appears in the calculation of the effective field as in the response of the ellipsoidal region to which that field applies.[43,58]

Sweet and Pettit[38] approached the solution in a somewhat different fashion. Their idealization of an "actual" model is shown in Figure 2.1. In the idealized system, the inclusions are replaced by ellipsoidal particles sufficiently isolated that the field in the matrix is essentially constant at a value $\overline{E}_m$. Then, the total field along the x axis is given by

$$\overline{E}_x = \sum_i f_i \overline{E}^x_{in}(i) + (1-f)\overline{E}_m \tag{2.13}$$

where

f_i = volume fraction of inclusions of type i,

$E_{in}(i)$ = x component of the constant field inside an ellipsoidal inclusion, and

f = total volume fraction of inclusions = $\sum_i f_i$

Assuming that the ellipsoidal inclusions have a scalar dielectric constant ε_c and are aligned with the principal axis along the x direction in a homogeneous medium with dielectric constant ε_m,[32,66] then

$$\overline{E}^x_{in}(i) = \frac{\varepsilon_m \overline{E}_m}{L_i \varepsilon_c + (1-L_i)\varepsilon_m} \tag{2.14}$$

where L_i = depolarization factor for the ith type particle.

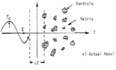

a) Actual Model

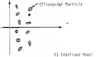

b) Idealized Model

Figure 2.1 Maxwell-Garnett theory idealized model of two phase (particle and matrix) composite.

Also, the average polarization may be written as

$$\overline{p} = (\sum_i f_i \overline{p}_i + (1-f)p_m)$$

$$= \frac{1}{4\pi} (\sum_i f_i (\varepsilon_c - 1) E_{in}(i) + (1-f)(\varepsilon_m - 1) E_m) \qquad (2.15)$$

Since $4\pi\overline{p} = (\overline{\varepsilon}-1)\overline{E}$ and $\overline{E}$ is given by equation (2.13), for $\overline{\varepsilon} \rightarrow \varepsilon_{MG}$, then

$$\varepsilon_{MG} = \varepsilon_m \left(\frac{1+\sum_i f_i (1-L_i)\alpha_i}{1-\sum_i f_i L_i \alpha_i}\right) \qquad (2.16)$$

where the polarization factors, α_i, are defined by

$$\alpha_i = \frac{\varepsilon_c - \varepsilon_m}{\varepsilon_m + L_i(\varepsilon_c - \varepsilon_m)} \qquad (2.17)$$

Equation (2.16) is the general equation derived by Sweet and Pettit[32] for ellipsoidal shaped inclusions. This reduces to the form shown in Equation (2.12)[43,55,62,64] proving that they are identical.

A theoretical model has been developed by O'Neill and Ignatiev[67] to deal with the case where the inclusions are assumed to be randomly distributed, both in orientation and in eccentricity. The resulting equation is much more complex than any of the above. Thus, although valid for the more general case of randomly distributed orientation and eccentricity, its usage is restricted because of its complexity.

The MG theory, as derived above, breaks down when the distance between inclusions become small, i.e., the inclusions are no longer isolated. Thus, for volume fractions of inclusions ≥ 0.1, the Maxwell-Garnett theory needs modifications[32,43]. Furthermore, actual films, such as black chrome films, have surface roughness variations, which add to the error resulting from the model.[32,68,69]

One approach[32,68,70,71] to overcome this problem of higher volume fraction of inclusions is to model the inclusions as coated spheres, consisting of a core with dielectric constant ε_c surrounded by the coating with dielectric constant ε_s. The dielectric constant ε_{cs} of such spheres is then calculated based on the ratio of the core volume to total particle volume. Other approaches have also been utilized.[72-74] These involve assuming that the particles are very small, of arbitrary shape or have an arbitrary distribution. Thus, the nature of the assumptions restrict each model to a narrow range of film structure.

Reflectivity Curves

In order to obtain reflectance values, relations between the dielectric constants and the refractive index are utilized, viz., the complex dielectric function is given by

$$\varepsilon = \varepsilon_a + \hat{j}\varepsilon_b \qquad (2.18)$$

The index of refraction is given by

$$\tilde{n} = n + \hat{j}k \qquad (2.19)$$

and

$$\tilde{n} = \varepsilon^{1/2} \qquad (2.20)$$

$$\varepsilon_a = n^2 - k^2 \tag{2.21}$$

$$\varepsilon_b = 2nk \tag{2.22}$$

The values for n and k for chromium as a function of wavelength have been reported[75-77] Several values for Cr_2O_3 have been reported[51,78-81] depending on the form of Cr_2O_3 The values most frequently chosen are those for crystalline Cr_2O_3 since even a short thermal aging sequence has been reported to cause crystallization of the initially amorphous Cr_2O_3[32,55] The refractive index of Cr_2O_3 used in this study is[32,80]

$$n_{Cr_2O_3} = 2.5 \quad \text{and} \quad k_{Cr_2O_3} = 0$$

Scanning electron photomicrographs of electrodeposited black chrome films reveal that the agglomerates are approximately spherical in shape (see following chapters) Thermal exposure of these black chrome films does not significantly change the size of the spherical agglomerates. Reported data suggest that thermal exposure of black chrome containing nonspherical Cr particles tends to drive them towards a spherical shape[31,82] Therefore, assuming that the inclusions are spherical ($L_i = \frac{1}{3}$ for all i) is reasonable. All the calculations will be made using this assumption although the effect of eccentricity will be discussed where necessary

The calculation of reflectance as a function of wavelength is accomplished using Rouard's method, described in detail by Heavens,[83] Chang and Hall[52] and Sweet and Pettit.[32] This involves defining the film as being composed of a series of layers, each with its own uniform dielectric constant. The reflectance is then obtained by the interaction of these layers, each of constant refractive index, with light As is evident, the method assumes that the film can be characterized by a layered structure, an assumption that is not necessarily valid for black chrome films. The calculation requires detailed information on the relative volume fraction of metallic Cr and Cr_2O_3 as a function of depth into the film.

Model Calculations

Calculations of ε_{MG} and ε_B were performed using the equations developed in the preceding sections and Appendix A, specifically, equations (2.16) and (A-3). The refractive indices of Cr that were used are those derived by Sweet and Pettit[32] from data reported by Johnson and Christy[75] and Barker and Ditzenberger.[76] Sweet and Pettit obtained the refractive index, plotted in Figure 2.2, by smoothly joining the data reported elsewhere.[75,76]

Due to the nature of the solar energy spectrum (Figure 1.1), the wavelength range of primary interest is $0.2\ \mu m < \lambda < 2\ \mu m$. Calculations will, therefore, be done at representative wavelengths within this range.

Model A

The first model chosen consists of spherical Cr particles embedded in a medium of air ($\varepsilon_m = 1$). Equations (2.16) and (A-1) were then used to calculate the dielectric constant as a function of volume fraction of Cr. These are plotted in Figures 2.3 - 2.5 for wavelengths of 0.5, 1.0 and 2.0 μm, respectively. The figures show that the effect of the volume fraction of Cr is different for the two theoretical approaches (BEM and MG). The dielectric constant from the BEM approach, ε_B, shows a much

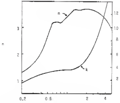

Figure 2.2 Real, n, and imaginary k, parts of the complex index of refraction for Cr (from ref. 32).

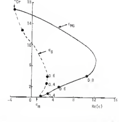

Figure 2.3 Effect of the volume fraction of spherical Cr inclusions in a medium of air on the dielectric constant at a wavelength of 0.5 μm. ϵ_B is the Bruggeman dielectric constant and ϵ_{MG} is the Maxwell-Garnett dielectric constant.

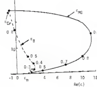

Figure 2.4 Effect of the volume fraction of spherical Cr inclusions in a medium of air on the dielectric constant at a wavelength of 1 μm

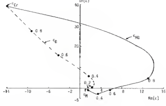

Figure 2.5 Effect of the volume fraction of spherical Cr inclusions in a medium of air on the dielectric constant at a wavelength of 2 μm.

more rapid increase in the imaginary component that is responsible for absorption. Absorptances computed using the BEM approach are always higher than those predicted by the MG theory. This is true for intermediate volume fractions. As expected, however, as $f_{Cr} \rightarrow 0$, ϵ_{MG} and $\epsilon_B \rightarrow \epsilon_M$, and as $f_{Cr} \rightarrow 1$, ϵ_{MG} and $\epsilon_B \rightarrow \epsilon_{Cr}$.

It should be noted that a similar variation of the dielectric constant will be observed for Cr particles in a medium that may not be air but is not insulating. For example, Cr particle distribution in an insulating, non-absorbing medium of Cr_2O_3 ($\epsilon = 6.25$) will result in dielectric constant-volume fraction plots similar to those plotted in Figures 2.3 - 2.5, only the values will be different.

The large difference between ϵ_{MG} and ϵ_B at $0.2 \lesssim f_{Cr} \lesssim 0.9$ is due to the percolation phenomena.[43] This refers to the sudden onset of electrical conduction at a critical volume fraction of conducting material in an insulating matrix. In the dielectric medium case, this is equivalent to $\left|\frac{\epsilon_c}{\epsilon_m}\right| \rightarrow \infty$, where ϵ_c refers to the dielectric constant of the inclusion. The BEM theory predicts that the threshold occurs at ~ 33% conducting material, while the MG theory predicts a finite conductivity for any non-zero value of volume fraction conducting material.[43] Experimental evidence suggests that the threshold occurs with $\gtrsim$ 15% conducting material.[54] Since the appearance of conductivity at the percolation threshold requires near-contact of metallic particles, the presence of non-spherical inclusions will favor conduction at lower volume fractions than that predicted by the BEM theory.

Microstructural studies[31,35,50,51,54,55,86] reveal that the black chrome coatings consist of approximately spherical agglomerates with diameters ranging from 500 - 2000 Å These agglomerates have been reported to contain metallic Cr crystallites of 100 - 1000 Å in size The distribution of spherical agglomerates (and Cr crystallites) in the matrix is clearly not topologically equivalent as required in the fundamental SEM theory approach, which assumes that the constituents of the composite are topographically symmetrical.

A comparison of the volume fraction dependence of several models[32,71,73,74,87] of a composite medium with a periodic array of inclusions shows that their dielectric constant is similar to that obtained with the MG theory. It is to be noted that this comparison is valid only for the composite in which the inclusions are isolated from each other Therefore, the MG theory can be utilized for calculating the dielectric constant of black chrome films provided the inclusions effect on the dielectric constant is independent for each included particle

The data in Figures 2.3 - 2.5 were plotted for a distribution of spherical Cr particles For non-spherical particles, absorption will be affected by the distribution of the eccentric particles. Van de Hulst[88] showed that the presence of highly eccentric inclusions with the long axis in the plane of the film will increase absorption at a given wavelength since such particles are more easily polarized than spherical particles Application to the data plotted in Figures 2.3 - 2.5 means that ϵ_{MG} shifts to lower real ϵ and higher imaginary ϵ as the ratio of the long axis to the short axis increases

Model B

The second model for which the dielectric constant is calculated is schematically shown in Figure 2.6. The metallic Cr particles of model A are replaced by coated spheres in model B. Each coated sphere consists of a core of metallic Cr surrounded by dense Cr_2O_3. The dielectric constant of the coated sphere, ϵ_{cs}, is computed and utilized in equations (2.16), (2.17) and (A-3). ϵ_B, calculated with equation (A-3) is plotted for comparison only, it is not used for further computation. The coated sphere's dielectric constant is calculated from[72]

$$\epsilon_{cs} = \epsilon_{Cr_2O_3} \left[\frac{2\epsilon_{Cr_2O_3}+\epsilon_{Cr}+2\Omega\,(\epsilon_{Cr}-\epsilon_{Cr_2O_3})}{2\epsilon_{Cr_2O_3}+\epsilon_{Cr}-\Omega\,(\epsilon_{Cr}-\epsilon_{Cr_2O_3})}\right] \qquad (2.23)$$

where Ω is the ratio of the core volume to the total coated sphere volume.

The dielectric constant for model B, calculated for a composite with the insulating medium having $\epsilon = 1$, is plotted in Figures 2.7 and 2.8. The data in Figure 2.7 show the variation of ϵ with Ω at 1 μm for a volume fraction of coated sphere of 0.5, while data in Figure 2.8 show the volume fraction dependence of ϵ at $\Omega = 0.4$ and 1 μm. The data show that ϵ is sensitive to both Ω and volume fraction of coated spheres.

The data were calculated assuming that the insulating medium had a dielectric constant of unity. In black chrome films, however, the matrix is expected to be a composite of initially deposited Cr_2O_3 and voids. The structure of black chrome film agglomerates is, therefore, more likely to be similar to the schematic illustration of Figure 2.9. The coated spheres of Cr metal surrounded by a passivating layer of Cr_2O_3 are distributed in a matrix of voids and as-deposited (amorphous) Cr_2O_3

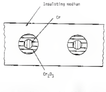

Figure 2.6 Schematic illustration of Model B coated spherical particles embedded in an insulating medium

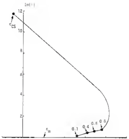

Figure 2.7 Effect of Ω on the Maxwell-Garnett dielectric constant at a wavelength of 1 μm for a volume fraction of coated sphere = 0.5 in a medium of air.

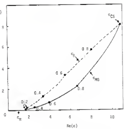

Figure 2.8 Effect of volume fraction of coated sphere with $\Omega = 0.4$ in a medium of air at a wavelength of 1 μm

Since this matrix differs from an air matrix, the computed ε_{MG} will be different. For example, ε_{MG} for a composite system with $\Omega = 0.4$ and $f_{cs} = 0.4$ immersed in a matrix of Cr_2O_3 at 1 μm wavelength would be $(10.2 + \hat{j}\,5.9)$ instead of $(6.4 + \hat{j}\,2.16)$, as computed for air medium (Figure 2.8). The two values of ε_{MG} listed above represent extreme cases. Plotting the computed values of ε_{MG} for a Cr_2O_3 matrix shows that the curve for ε_{MG}, plotted in Figure 2.8, shifts slightly to the right for intermediate volume fractions of coated spheres.

The model structure shown in Figure 2.9 draws support from experimental evidence presented in the following chapter and from published results.[31,35,50,51,54,85,86] The oxidation behavior of black chrome films suggests that the as-deposited oxide is porous and non-passivating (or only weakly so). The oxide that forms on thermal exposure forms a passivating coating around the metallic Cr particles. The thickness of the passivating oxide layer is a function of the temperature. It is possible to estimate the thickness of this layer from data on pure Cr oxidation, as will be explained in later chapters.

The two models discussed above are by no means the only two possible. Chromium metal distribution in the matrix can be modeled in a number of different ways.[31,32,52] However, most of them are unsatisfactory for explaining black chrome behavior since the models are either too simplistic (e.g., distribution of uniform sized cubes of Cr) or topologically quite different from experimental evidence.

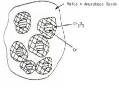

Figure 2.9 Schematic illustration of possible structure of black chrome film aggregates

Reflectance Calculations

The calculation of reflectance from the dielectric constant requires knowledge about the variation of the constituents as a function of depth into the film. For black chrome films, this requires knowledge about the distribution of Cr_2O_3, Cr and voids. It also requires knowledge of the total void volume. The volume and distribution of voids in black chrome films are extremely difficult to determine. Therefore, voids are assumed to be uniformly distributed. The size of these voids is also important. Since void volume in black chrome films has been estimated to be large,[32] the voids are assumed to be large enough to act as part of the continuous matrix.

Reflectance calculations are made using Rouard's method [32,52,83] This involves dividing the film into a number of parallel segments (starting from the substrate) and assuming that each segment has a constant and uniform refractive index. The reflectance of the film is computed in a sequential manner, starting from the substrate. The complex reflectance (or Fresnel coefficient) is given by[32,52,83]

$$\bar{F}_k = \frac{\bar{R}_k + \bar{F}_{k+1}\exp(-2j\delta_k)}{1+\bar{R}_k\bar{F}_{k+1}\exp(-2j\delta_k)} \qquad (2.24)$$

where $\bar{R}_k$ is the ratio of the reflected to incident electric field strength at the interface between the (k-1) and kth layers, $\bar{F}_{k+1}$ is the Fresnel coefficient for the (k+1) layer, $\delta_k = 2\pi d_k \bar{n}_k/\lambda_o$, d_k is the thickness of the kth layer, $\bar{n}_k$ is its refractive index and λ_o is the wavelength for which reflectance is being determined. The stack (or total film) reflectance is given by

$$R = \tilde{F} \cdot \tilde{F}^* \qquad (2.25)$$

where $\tilde{F}^*$ is the complex conjugate of $\tilde{F}$

Swett and Pettit[32] have used the variation of the volume fraction ratio of Cr to (Cr + Cr_2O_3) as a function of depth shown in Figure 2.10. These calculated Ω's are based on the assumption that the ratio of Cr to (Cr + Cr_2O_3) (i.e., Ω) in the as-deposited films increases in a manner given by

$$\Omega(x) = \Omega_{max}(1-e^{-x/x_0}) \qquad (2.26)$$

where Ω_{max} and x_0 are parameters. The average film ratio, $\overline{\Omega}$, is related to Ω_{max} by

$$\overline{\Omega} = \Omega_{max}[1-(\frac{x_0}{L})(1-e^{-L/x_0})] \qquad (2.27)$$

where L is the film thickness. For thermally exposed films, they assumed that Ω increases linearly with increasing depth into the film. The relations were arrived at by Sweet and Pettit[32] from Auger sputter profile data (see Chapter V) after making a number of assumptions.[89,90] However, the two most important assumptions are that there is no preferential sputtering of either Cr or Cr_2O_3 and sputtering of the films is not interfered with by the distribution. Evidence (see Chapters V and VI) suggests that Cr_2O_3 sputters almost twice as fast as metallic Cr. Therefore, the relations used by Sweet and Pettit[32] are not quantitative. However, the reflectance curves so computed suggest qualitatively (and semi-quantitatively) the correlations with volume fraction of Cr_2O_3 in the film.

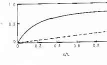

Figure 2.10 Relative volume fraction Cr to (Cr + Cr_2O_3), given by Ω, as a function of depth into the film (ref. 32)
—— as-deposited
- - - 3682 h at 400°C

Reflectance curves calculated by Sweet and Pettit are reproduced in Figure 2.11. The curves show that with increasing $\overline{\Omega}$ (from 0.2 to 0.5), the absorption edge shifts to longer wavelength. Furthermore, the broad interference peak at ~ 1.0 μm decreases with increasing $\overline{\Omega}$. This agrees with reflectance curves measured experimentally on black chrome films (see Chapter IV). Calculation of α_s values from the computed reflectance curves, such as those shown in Figure 2.11 predict that α_s should remain relatively constant until the volume fraction of Cr_2O_3 is ≥ 70%. This is plotted in Figure 2.12. This agrees reasonably well with experimentally observed data (see following chapters). At low volume fractions of Cr_2O_3 ($\lesssim$ 0.6), the model predicts relatively small changes in α_s. But, experimental evidence (see following chapters) shows that for Cr_2O_3 content $\lesssim$ 40%, α_s decreases rapidly. Sweet and Pettit ascribe this to the insensitivity of the reflectance curve to the form of $\Omega(x)$ used in computing them. They observed little difference in reflectance when calculated for low oxide content films with linear and exponential forms of $\Omega(x)$, i.e., their relationships are not valid at low Cr_2O_3 fractions. There may be another reason for the discrepancy. Some of the films with low oxide content (see later chapters) were observed to be much more dense. Therefore, computations of reflectance from ε_{MG} at low Cr_2O_3 fractions may need modification to include changes in void volume.

Some of the experimentally observed reflectance curves (see Chapter IV) did not show the broad interference peak at ~1.0 μm. Instead, with increasing thermal exposure, the reflectance increased almost uniformly at wavelengths below the absorption edge. Reflectance curves showing this behavior were computed by Sweet and Pettit[32] using the same procedure

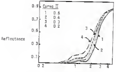

Figure 2.11 Spectral reflectance of a black chrome coating with Model B structure (ref. 32).

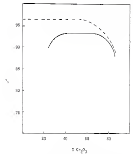

Figure 2-12 Comparison of the solar absorptance variation as a function of Cr_2O_3 content in the film between experimentally observed (solid line) and computed (dotted line, ref 32) values

(explained above), but with a different film model. This model, schematically illustrated in Figure 2.13, shows that the void plus amorphous oxide matrix has both Cr metal inclusions and Cr_2O_3 inclusions. Such a model requires that the as-deposited oxide must completely passivate the Cr metal particles that remain virtually unchanged on thermal exposure. At the same time, the as-deposited oxide must not passivate Cr particles that are oxidized on thermal exposure. Such behavior is not very likely. The formation of Cr_2O_3 on thermal exposure may be explained on the basis of experimental evidence presented in later chapters. The Cr_2O_3 crystallites may have been formed by the complete oxidation of Cr particles that were too fine in size to form a passive Cr_2O_3 coating without getting completely oxidized. Experimental evidence suggests that films that showed uniformly increasing reflectance below the absorption edge may have contained some small (~ 100 Å) Cr particles in the as-deposited condition. These would have been completely oxidized on thermal exposure whereas the larger Cr particles would form a passive Cr_2O_3 coating with thermal exposure. The model of Sweet and Pettit (Figure 2.13) does not agree well with experimental evidence. A more realistic model would be one wherein the as-deposited film contained Cr particles of fine sized (~ 100 Å) and relatively large sized (≥ 500 Å). On thermal exposure, the fine sized particles must be completely oxidized whereas the large sized particles would form a passive Cr_2O_3 layer around them. It should be noted that such a model complicates the computational process by necessitating the incorporation of another variable, uneven sizes of the constituents (Cr and Cr_2O_3) in the matrix. This makes the application of the MG (or BEM) theory more unsatisfactory.

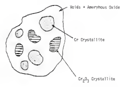

Figure 2.13 Schematic of model structure used to compute reflectance curves that show uniform increase in reflectance with thermal exposure (ref. 32)

Uncertainties in Model Calculations

Differential Sputtering Effects

The derivation of reflectance, based on the assumptions made by Sweet and Pettit,[32] is not very satisfactory in that the effect of differential sputtering rates of Cr versus Cr_2O_3 has been ignored. However, Cr_2O_3 has been observed to sputter at approximately twice the rate of metallic Cr. Comparison of the variation of Ω as calculated by Sweet and Pettit[32] (Figure 2.10) with experimentally observed data (Chapters V and VII) shows that there are marked differences. These differences are due to the differential sputtering effect and the variation of Ω in a manner dissimilar to that modeled by Sweet and Pettit. Analysis of Auger sputter depth profiles (Chapter V) suggests that Ω for thermally exposed films can be better modeled as follows: the thickness of the almost pure Cr_2O_3 outer layer increases with increasing oxide content and, secondly, the remainder of the film where Cr_2O_3 decreases with depth may be approximated with an exponential expression similar to that of Sweet and Pettit[32] (for the as-deposited film). The values of the different parameters in the two equations, however, are not constant but vary with thermal exposure. Thus, calculation of Ω from experimentally obtained Auger sputter data is likely to give more accurate results than the continuous fitted functions used by Sweet and Pettit.

Effect of Surface Roughness

The calculated values of roughness from the dielectric constant also suffer because roughness effects were ignored. Pettit and Sowell[8] reported a 5-6% increase in the solar absorptance of black chrome coatings deposited on rough substrates (1 - 2 μm scale irregularities) over those deposited on smooth substrates. The thermal emittance, however, showed little change. The surface roughness of the nickel-plated plain carbon steel substrates used in this study was comparable to the film thickness (Chapter IV). Auger sputter data (Chapter V) also show a broad substrate-film interface, due primarily to the substrate roughness. Although model calculations have ignored surface roughness effects, comparison is not affected since the error introduced is the same for all the films. This is because the substrate roughness shows little change with thermal exposure.

Effect of Voids and Agglomerate Size

In all the calculations, the effect of agglomerate size and void distribution on the reflectance has been ignored. By ignoring these effects, optical trapping due to the difference in refractive index between air and Cr_2O_3 has not been considered. Optical trapping refers to the absorption of incident radiation by a material due to the direction of scattering, the direction of scattering depends on the shape (and size) of the different constituents and their relative refractive indices. Such effects can be ignored only when comparing films that have the same void volume, void distribution and agglomerate size. Void content of as-deposited films containing ~ 40% Cr_2O_3 has been estimated to be ≥ 60%.[32] However, films with low oxide contents were observed to be much more dense (see later chapters). For films that have particles (Cr metal) distributed in a medium of air (model A), changes in the void volume result in changes in the volume fraction of the medium, the dielectric constants, resulting from such changes in a film, are shown in Figures 2.3 - 2.5. For black chrome films where the medium is a composite of Cr_2O_3 and voids, changing the void volume changes the effective dielectric constant of the medium. For example, at 1.0 μm wavelength and 50% Cr, ϵ_{MG} (equation (2.16)) is (10.93 + j 11.385) for no voids and (3.88 + j 0.718) for 100% voids, i.e., air medium. Similarly, changing the void distribution affects the dielectric constant of the film. Non-uniform void distribution also increases the complexity of reflectance calculations, since the refractive index of each segment of the film must be suitably altered to reflect that change. Because of the difficulty in determining the void volume or its distribution, all the calculations assumed constant void volume and uniform distribution. These assumptions introduced a systematic but constant error and therefore are reasonable for black chrome films that were deposited under similar conditions.

Changes in agglomerate size can also affect the dielectric constant. As for the voids, such changes are not easy to describe exactly by theoretical calculations. This is because optical trapping effects depend on the distribution of the components in the medium and their relative concentrations. For relatively large void volumes (and their uniform distribution), variation in agglomerate size from 500 - 2000 Å from film to film (but uniform within each film) is unlikely to cause large changes in reflectance. Black chrome films which have the same volume fraction of solids (Cr + Cr_2O_3) can have different agglomerate sizes only by varying the volume of voids within the agglomerate. For example, films with larger agglomerates will have higher void volume inside the agglomerate (and less between agglomerates) than films with smaller agglomerates. Computation of changes in reflectance based on changes in agglomerate size is extremely difficult since assumptions have to be made about the void size and distribution within the agglomerate and also the effect of changing void volume between agglomerates.

Incorporation of the effects of void volume, distribution and agglomerate size (and size distribution) are very difficult. The non-incorporation of such effects in model calculations is, therefore, a limitation; the severity of these limitations is not easy to estimate. However, comparison of experimental results with model calculations suggests that for films with ≥ 30% Cr_2O_3, reasonably good correlations can be achieved.[32] However, films with low Cr_2O_3 content exhibit distinctly different behavior from that predicted by such models.

Uncertainty in the Refractive Index

The dielectric constant is calculated from reported values of the refractive index for Cr and Cr_2O_3.[32,51,75-81] There is some disagreement in the reported values for both Cr and Cr_2O_3. The dielectric constant of Cr_2O_3 is closely related to the type of Cr_2O_3 (thin film, amorphous, crystal orientation, etc.).[51,78-81] The real part of the dielectric constant has been reported to range from 5.7 - 6.3, while the imaginary part has been computed to be $\leq 5 \times 10^{-3}$. Therefore, ignoring the imaginary part is not unreasonable. The choice of the real part of the dielectric constant of Cr_2O_3 certainly affects the dielectric constant of the composite. For example, calculation of ϵ_{MG} for model A type structure with Cr inclusions distributed in a medium of Cr_2O_3 give different results depending on the choice of Cr_2O_3 dielectric constant. At 1.0 μm and for 50% Cr, ϵ_{MG} is (10.825 + j 10.735) for $\epsilon_{Cr_2O_3} = 6.25$. This in turn will affect any reflectance values calculated from the dielectric constant which, in turn, affects the computed solar absorptance. From the calculated values of ϵ_{MG} for $\epsilon_{Cr_2O_3}$ values of 5.8 and 6.25, it can be predicted that higher solar absorptance would be obtained with $\epsilon_{Cr_2O_3} = 5.8$. This is because of the higher value of the imaginary coefficient of ϵ_{MG}. Such variations (in $\epsilon_{Cr_2O_3}$) are expected to cause variations in the solar absorptance of < 5%.

The dielectric constant of Cr was determined from reported values of the refractive index as a function of wavelength.[32,75,76] There is disagreement between the reported values. Variations of 7 - 15% in the refractive index values reported have been observed.[75] These variations have been attributed to surface preparation, presence of an oxide on the surface, film thickness, etc. Thus, calculation of the dielectric constants from these refractive indices will result in values that vary by about the same extent (5 - 15%). Calculation in the solar absorptance is thus likely to vary by about the same extent (5 - 15%). The reduction of such inaccuracies can only be achieved by using more accurate refractive indices than presently available.

Effect of Structure on Thermal Emittance

The thermal emittance of black chrome absorbers (Chapter I) is largely determined by its interaction with radiation at long wavelengths (≥ 2 μm). Since these films are typically ≥ 0.2 μm thick, their interference with long wavelength radiation is quite small. The major influence on the thermal emittance is the interaction with the substrate. The high reflectance of metal substrates is the primary reason for the relatively low thermal emittance of these absorbers. Although film thicknesses of the order of 10 μm have been reported to be necessary to cause a sharp increase in emittance,[12] thinner films can also increase emittance (beyond that of the substrate). Comparison of thermal emittance date on different black chrome films (Chapter IV) shows that films that are thicker than ~ 0.2 μm, do increase their emittance. This is because the increased black chrome films thickness causes a shift in the absorption edge to longer wavelengths (Chapter IV).[55] A fraction of the thermal emittance is from this wavelength range (≲ 2 μm). Thus, emittance increases even when film thicknesses are ≳ 0.2 μm, the extent of increase is, however, not as great as that observed for thicker films.

Conclusions

The MG theory can be extended to predict the behavior of black chrome films electrodeposited onto metal substrates. Modeling the film structure as having coated spheres distributed in an insulating medium of air (or similar material) improves the correlations between theoretical predictions and experimental observations. The BEM theory, however, appears unsuited for application to black chrome films primarily because of the nature of the distribution of the constituents in the coatings.

The microstructural model comprised of a sphere of Cr coated with dense Cr_2O_3 embedded in a matrix of voids and amorphous Cr_2O_3 gives dielectric constant values that predict reflectance (and absorptance) values similar to those observed. However, due to the many assumptions involved in each step of the calculation, the results must be viewed as being essentially semi-quantitative. Increased quantification requires significant input from experimental results, e.g., Auger sputter profile results. Incorporation of the effects of void volume and distribution and agglomerate size and size distribution are very difficult. The non-incorporation of such effects in model calculations is, therefore, a limitation. Furthermore, the severity of these limitations is not easily estimated. Comparison of experimental results with model calculations suggests, however, that for films with ≥ 30% Cr_2O_3, reasonably good correlations can be achieved.[32]

The thermal emittance, unlike the solar absorptance, is only slightly affected by the black chrome film. The reflectance properties of the substrate are of more significance. However, thicker black chrome films show increased thermal emittance due to a shift in their absorptance edge to longer wavelengths.

Pages
are
misnumbered
following
this
insert

CHAPTER III
ELECTRODEPOSITION

Introduction

Electrodeposited black chrome films have been used in both flat plate and mid-temperature concentration collectors [6,91] Although initial research indicated that the coatings would maintain their high solar absorptance and low thermal emittance during extended use at temperatures ≥ 250°C, field data proved otherwise [6,25] The thermal stability of black chrome coatings has, therefore, been the subject of recent studies [8,13,15,26,36,40,62,92] Results indicate that there is a significant correlation between the electrodeposition bath composition and the deposition conditions with the stability of the coatings Although several baths have been utilized for the electrodeposition of black chrome,[12,25] the one most commonly used is the Chromonyx bath developed by the Harshaw Chemical Company [36] The substrate can be a variety of metals, but is typically plain carbon steel that has been plated with a metal with high white reflectance, typically nickel ~ 25 μm thick [82,92]

The goal of this study is to determine the effect of the bath composition and the deposition conditions on the composition and optical properties of the black chrome deposits, both as-deposited and when subjected to thermal treatment at temperatures above 250°C

Experimental Procedure

Black chrome films were electrodeposited from a modified Chromonyx bath onto plain carbon steel substrates previously electroplated with nickel. The sequence followed during deposition is described in Appendix B. This procedure has been adapted from that suggested by Pettit and Sowell [32]. Briefly, the procedure involved etching the substrate to get a smooth surface and then cleaning it with both acidic and basic reagents prior to deposition. Typical surface roughness of the substrate after etching is shown in Figure 3.1. A Dektak profilometer was used to generate the surface profile. It was essential to prevent drying of the substrate during the cleaning sequence to avoid poor adhesion. Cleaning and plating solutions were also changed frequently to ensure their effectiveness and composition.

The black chrome deposition apparatus is shown schematically in Figure 3.2 while the details of the substrate holder are shown in Figure 3.3. The bath was contained in a low density polyethylene container, as were most of the other solutions. The anode was made of mild steel of a size sufficient to give an anode-to-cathode (sample) surface area ratio of greater than 2:1. The power supply used was a DC source having a 0 - 30 V, 0 - 30 A range. The chemicals used were as follows:

1) Chromic Acid, anhydride - purified grade (or better), Fisher Scientific
2) Acetic Acid, glacial - reagent grade, Fisher Scientific
3) Oxalic Acid, crystals - analytical reagent, Mallinckrodt
4) Iron Oxalate - reagent grade, Reidel
5) Barium Carbonate, powder - reagent grade, J. T. Baker

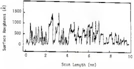

Figure 3.1 Surface roughness profile of etched nickel-plated mild steel substrate taken with a Sloan Dektak profilometer

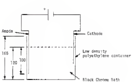

Side View

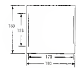

Top View

Figure 3.2 Schematic of the black chrome electrodeposition apparatus [all dimensions in mm].

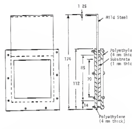

Figure 3.3 Schematic of cathode holder with substrate in place
[all dimensions in mm]

Other chemicals used, such as sulfuric acid, ferrous ammonium sulfate, etc., were all of reagent grade obtained from Fisher Scientific Company. The use of high purity grades reduces possible effects due to impurities.

Barium carbonate was added to the bath to concentrations of about 8 g/l to ensure that any sulfates present were precipitated out as barium sulfate. Dissolved sulfates have been reported to reduce the current density range over which black chrome deposits can be obtained.[36]

Silver nitrate was also added to the bath to control the build up of chloride ions in solution. Pettit and Sowell[92] observed low solar absorptance and poor thermal stability with increased chloride ion concentration above about 15 mg/l. Small amounts of silver nitrate were added periodically to control the chloride ion concentration below 10 mg/l.

Experimental Variables

Although a large number of variables are involved in any electrodeposition process, the most important variables in black chrome depositions have been reported to be the following:[36,82-92]

1) Cr^{+3} concentration,
2) chromic acid concentration (CrO_3),
3) addition agent concentration,
4) Fe^{+3} concentration, and
5) current density

Pettit and Sowell[92] reported that the optimum conditions for black chrome deposition were as follows:

CrO_3	332 ± 4 g/l
Addition Agent	27 vol %
Cr^{+3}	8 ± 0.5 g/l
Fe^{+3}	7.5 ± 1 g/l
Current Density	188 mA/cm^2 for 5 minutes

The addition agent listed above is a proprietary agent of the Harshaw Chemical Company However, the most important constituent of the addition agent is believed to be acetic acid[93] Pure acetic acid was used for the addition agent in all of the depositions for this study

The number of experiments required to vary all the parameters over a broad range would be very large Therefore, to reduce the number of experiments without a significant decrease in confidence levels, a statistical design of experiments using random number approach was utilized[94] This involves listing the various combinations of deposition parameters and then choosing specific combinations of parameters with the aid of random number tables

The bath composition was analyzed using the procedure given in Appendix C Chromic acid, acetic acid, Fe^{+3} and Cr^{+3} concentrations were analyzed in this fashion

Sequence of Experiments

The sequence for electrodeposition chosen was to start with a low Cr^{+3} and low Fe^{+3} concentration bath and gradually increase their levels according to the experiments chosen The conditions under which the black chrome samples were deposited are listed in Table 3 1 It should be noted

Table 3.1 Electrodeposition Conditions* for the Black Chrome Films Deposited onto Nickel Plated Steel

#	Sample Number	Cr^{+3} (g/l)	Fe^{+3} (g/l)	Chromic Acid (g/l)	Acetic Acid (vol %)	Current Density mA/cm²	Deposition Time (minutes)
1	19C	3.65	0.22	198.2	21.69	176.5	5
2	19F	4.9	0.34	191.7	21.34	210.6	4.54
3	20A	4.9	0.66	194.1	21.47	182.9	8
4	20B	6.2	0.34	184	25.5	193.4	5
5	20C	6.2	0.36	181.1	25.28	178.5	8
6	20D	6.2	0.39	184.4	23.4	208.3	5
7	21A	8.4	0.34	179.7	24.74	178.6	8
8	21B	8.1	0.39	173	27.3	191.2	5
9	21C	8.1	0.42	176.3	27.2	205.9	5
10	22A	9.5	0.45	171.8	26.9	205.9	5
11	22B	9.5	0.50	171.8	27.17	189	5
12	29Ba	5.4	4.41	384.2	20.14	176.4	5
13	29C	5.5	4.41	388.7	20.31	193.3	5
14	29D	5.5	5.30	414.3	18.14	193.3	7.5
15	29E	5.5	7.26	413.1	17.54	198.1	10
16	29F	5.5	7.61	404.5	19.25	216	7.5
17	29J	~5.5†	6.09	361.1	24.94	182.4	10
18	37A	4.95	3.49	284	26.45	163.3	10
19	37B	6.2	3.57	287.7	28.22	183.7	5
20	37C	5.1	3.57	299.6	25.16	193.9	5
21	37D	6.0	3.02	348.1	19.61	193.9	7.5
22	37E	5.1	3.04	366.6	14.16	193.9	10
23	37F	5.45	3.74	301.3	26.18	204.1	7.5
24	37Q	8.5	6.92	306.2	26.84	183.7	5

* Temperature of the bath maintained at 20-26°C, except for #14, where the temperature was 27°C, and #15 and 17, where the temperature reached 26°C

† The Cr^{+3} concentration of #17 was not determined, it is expected to be between 5.5 and 6.0 g/l.

that all the samples were not made from the same bath. The 37 series depositions were made with a fresh bath while the 29 series were made from the same bath as that used for the 19-21 series depositions, but only after dilution and appropriate additions.

The addition of iron oxalate and oxalic acid were made according to the following equations:

$$FeC_2O_4 \cdot 2H_2O + CrO_3 + H_2O \rightarrow Fe(OH)_3 + Cr(OH)_3 + 2CO_2 \qquad (3.1)$$

$$3H_2C_2O_4 + 2CrO_3 \rightarrow 2Cr(OH)_3 + 6CO_2 \qquad (3.2)$$

From equation (3.1) it is evident that 1 g of iron oxalate dihydrate reacts with chromic acid to give 0.31 g of Fe^{+} and 0.29 g of Cr^{+3}. From equation (3.2), 1 g of oxalic acid is seen to form 0.385 g of Cr^{+3}. Sufficient time was given after each addition for completion of the reaction (at least 30 minutes, or until the end of gas evolution) before the bath was used. The bath was sampled before or after each deposition for chemical analysis. These samples were analyzed later, using the procedure listed in Appendix C.

Results

The conditions under which the different black chrome samples were deposited are listed in Table 3.1. Chromic acid concentration was varied over a range of 171 - 414 g/l, acetic acid was varied from 14 - 28 vol %, Fe^{+3} from 0.2 - 7.6 g/l and Cr^{+3} from 2 - 10 g/l.

Although periodic additions of silver nitrate were made to control the chloride ion concentration in the bath, several of the black chrome films showed significant amounts of chlorine in them. This evidence is discussed in detail in Chapter V, which deals with the analysis of the black chrome films.

With the exception of black chrome films 21A, 21B, 21C, 22A and 22B, all the coatings were dark, ranging in color from dark blue to matte black. Coatings 21A through 22B, however, had a grayish-white appearance. The thickness of these films, as measured from Auger sputter data, was much less than that of the other films. These films also had very little oxide content. The details are discussed in Chapter V. The gas evolution during the deposition of these particular films was observed to be much less vigorous.

Black chrome films 29D, 29E and 29J, which were all deposited at temperatures of 27° or 28°C, had very rough appearances. The edges of the deposit were streaked. However, coatings 29C and 29F, which were deposited under similar bath conditions except that the bath temperature was < 25°C, did not show the streaked or rough appearance.

CHAPTER IV
OPTICAL PROPERTIES

Introduction

The two important optical properties are the solar absorptance (α_s) and the thermal emittance (ϵ). For a high efficiency converter, it is essential that α_s be large, while ϵ be small. These optical properties have already been defined in Chapter 1.

Measurement of Solar Absorptance

Solar absorptance values were obtained by first measuring the reflectance of the black chrome coatings as a function of wavelength. The absolute reflectance was calculated by the use of a reference white sample (see below). The reflectance thus obtained was then convereted to solar absorptance by integrating the wavelength-sensitive absorptance over the entire AM spectrum to obtain a single value for α_s. However, since a single number does not clearly show the wavelength-sensitive nature of the films, most of the data will be discussed on the basis of the reflectance curves.

The white reference sample used was Eastman 6080, obtained from Labsphere.[96] The true reflectance values of this coating are listed in Table 4.1. This procedure of calculating the solar absorptance from measurements of the reflectance is the principle of all the commercially available instruments.[12,96,97] Although the reflectance data reported here were determined with an instrument assembled locally, the principles used are identical to those used by the commercial instruments.[12,97]

Table 4.1 True (Absolute) Reflectance of Eastman 6080 White Reference Coating

Wavelength (nm)	Absolute Reflectance	Wavelength (nm)	Absolute Reflectance
250	0.939	1400	0.932
300	0.987	1500	0.929
400	0.995	1600	0.944
500	0.998	1700	0.939
600	0.998	1800	0.915
700	0.997	1900	0.829
800	0.996	2000	0.811
900	0.995	2100	0.842
1000	0.991	2200	0.842
1100	0.992	2300	0.816
1200	0.983	2400	0.768
1300	0.980	2500	0.703

The instrument used is shown in Figure 4.1 and consists of a quartz halogen light source, a grating monochromator (with appropriate gratings) and an integrating sphere and detectors (Si or PbS). The manufacturers are listed in the references [95,98]. The integrating sphere was also coated with the Eastman 6080 material, other details are shown in Figure 4.2. The procedure followed for the measurement of reflectance was as follows:

1) Place the black chrome sample (≥ 1x1 cm) in the sample holder and screw the holder into the integrating sphere opening.
2) Use the appropriate detector and grating depending on the wavelength range over which measurements are to be made (see Table 4.2).
3) If using the Si detector, connect to the electrometer, such as the Keithley 602B. Connect the output from the electrometer to a suitable x-y recorder. Also connect the output from the monochromator wavelength readout to the x-axis of the recorder. If the PbS detector is being used, connect the output to a high impedance ohmmeter and measure the change in resistance as a function of wavelength. Both the circuits are shown in Figure 4.3a and 4.3b.
4) Allow at least half an hour warm-up time for the electronic components.
5) Make zero adjustments on the electrometer and wavelength readout and select suitable x and y ranges on the recorder.
6) Switch on the lamp source and obtain the plot of detector signal versus wavelength. The input voltage of the lamp source is selected to give the highest signal within range for the reference sample.

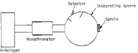

Figure 4 1 Schematic of the instrument used for measuring spectral reflectance

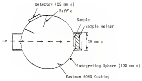

Figure 4-2 Details of the integrating sphere

Table 4.2 Instrument Settings for Measurement of Reflectance as a Function of Wavelength

Wavelength Range	Oriel Grating Number	Wavelength Scan Rate	Slit Size	Detector	Electrometer Full Scale Reading	Ohmmeter Full Scale
350-750 nm	7271	25 nm/min	0.8 mm	Si	0.03×10^{-8}A	--
700-1100 nm	7272	50 nm/min	0.8 mm	Si	0.1×10^{-8}A	--
1000-1500 nm	7272	--	3.2 mm	PbS	--	300 kΩ
1400-2500 nm	7273	--	3.2 mm	PbS	--	300 kΩ

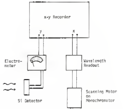

Figure 4 3a Circuit diagram for obtaining reflectance versus wavelength plots with a Si detector

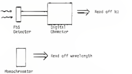

Figure 4-3b Circuit diagram for obtaining reflectance versus wavelength with PbS detector

7) The reference sample is then substituted for the black chrome and the above procedure repeated, except that the lamp source is not switched off between the two scans.
8) The procedure is repeated over the entire wavelength range of 0.3 - 2.5 μm.

Frequent alignment checks were made to ensure that there was no misalignment error introduced. Reflectance values for the black chrome films were then converted to true reflectance with the aid of Table 4.1. From the recorded data, the reflectance values were obtained at 50 nm intervals. For the wavelength range of 1000 - 2500 nm, the PbS detector output was measured at 100 nm intervals.

Measurement of Thermal Emittance

Thermal emittance was measured by using an instrument manufactured by Devices and Services Company.[99] The detector portion of the AE emissometer is heated to 180°F, while the sample is at room temperature. The detector is a differential thermopile, with aluminum foil and black paint as the sensing surfaces. This ensures a near constant linear response to wavelength from 3 - 30 microns. Two reference samples are provided with the emissometer, one with high and the other with low emissivity. Pettit and Mahoney[95] determined that the AE emissometer had an accuracy of ± 0.03 emittance units for black chrome at the detector temperature of 180°F (80°C). This compares favorably with the more expensive commercial units. The major limitation of the AE emissometer is that the sample must be at least 6x6 cm in size. This restricted our measurements on the black chrome films to the as-deposited condition.

since the thermally treated samples were smaller in size. Experimental limitations prevented deposition of samples greater than about 8x8 cm in size. Thermal aging tests required that the as-deposited samples be cut, resulting in smaller than 6x6 cm thermally aged samples.

The procedure followed for emittance measurement is quite straightforward. After the emissometer has been switched on for more than 30 minutes, the thermopile voltage for the two reference samples and the black chrome are measured. To ensure good conductivity, a drop of water is placed between the sample and the heat sink. The emissivity is then calculated from[99]

$$\text{emissivity}, \quad e = \frac{V_{\text{sample}} \times 0.93}{V_{\text{std.}}} \qquad (4.1)$$

where

V_{sample} = voltage measured off unknown

$V_{\text{std.}}$ = voltage measured off standard whose emissivity equals 0.93.

The measurement set up is schematically shown in Figure 4.4. The principle of the operation of the emissometer has been explained in detail elsewhere.[99]

Results

The results for the reflectance curves as a function of wavelength are plotted in Figures 4.5 to 4.13. Figure 4.8 shows data for the Ni-plated mild steel substrate. Several curves in each of the figures (4.6 - 4.13) are all for the same black chrome film, but after thermal exposure at the specified temperature and time. A selected few solar absorptance values,

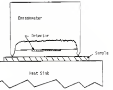

Figure 4.4 Schematic of instrument set-up for measurement of thermal emittance

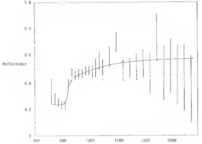

Figure 4.5 Reflectance of nickel-plated mild carbon steel substrate as a function of wavelength

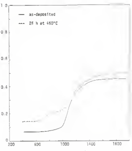

Figure 4.6 Reflectance of black chrome film 19F as a function of wavelength

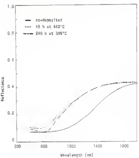

Figure 4-7 Reflectance of black chrome film 20C as a function of wavelength

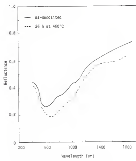

Figure 4.8 Reflectance of black chrome film 21A as a function of wavelength

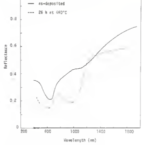

Figure 4.9 Reflectance of black chrome film 22A as a function of wavelength

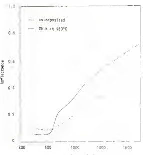

Figure 4.10 Reflectance of black chrome film 298a as a function of wavelength

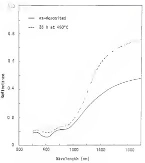

Figure 4.11 Reflectance of black chrome film 29C as a function of wavelength

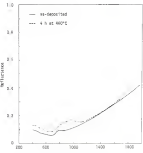

Figure 4.12 Reflectance of black chrome film 29E as a function of wavelength.

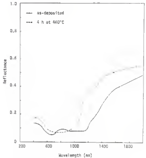

Figure 4.13 Reflectance of black chrome film 29F as a function of wavelength.

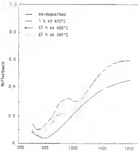

Figure 4.14 Reflectance of black chrome film 37A as a function of wavelength.

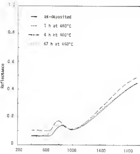

Figure 4.15 Reflectance of black chrome film 378 as a function of wavelength.

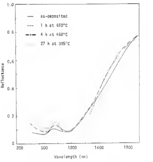

Figure 4.16 Reflectance of black chrome film 370 as a function of wavelength

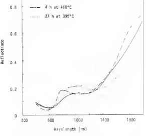

Figure 4.17 Reflectance of black chrome film 37E as a function of wavelength

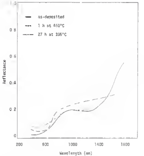

Figure 4.18 Reflectance of black chrome film 37F as a function of wavelength

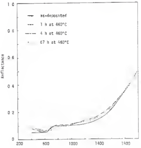

Figure 4.19 Reflectance of black chrome film 37Q as a function of wavelength.

calculated from the reflectance curves, are listed in Table 4.3 using both the AM0 and AM2 solar irradiance spectra. Emittance values, listed in Table 4.4, are for black chrome films in the as-deposited condition only since thermally exposed samples are too small for measurement with the emissometer.

Reflectance Measurements

The reflectance versus wavelength curves plotted in Figure 4.5 - 4.19 are the result of the smooth joining of the data points obtained with the procedure explained earlier and after consideration of the error range at each wavelength. For clarity, the error bars are only shown on Figure 4.5. They are, however, applicable to all the reflectance curves

The error bars shown on Figure 4.5, which is a plot of reflectance versus wavelength for the nickel substrate, were calculated from consideration of the following causes for uncertainty

a) Dark noise of the detector - for the silicon detector, dark noise was ≤ 1% of the reading, while for the PbS detector it was ≤ 10%.

b) Uncertainty in the measured value - typical silicon detector output signal as a function of wavelength is shown in Figures 4.20a and 4.20b for the wavelength ranges of 350 ~ 750 nm and 700 ~ 1150 nm, respectively, for both a black chrome sample and the reference white sample. The relative uncertainty in the measured value of intensity is, thus, a function of wavelength. For example, from Figure 4.20b, uncertainty in the measured value at 900 nm is a smaller fraction of the true value than

Table 4.3 Solar Absorptance (α_s) Calculated from the Reflectance Curves Using the AM0 and AM2 Solar Irradiant Spectra

Solar Irradiance Used	20C		29E		37Q	
	As-Deposited	45 hours at 460°C	As-Deposited	4 hours at 460°C	As-Deposited	67 hours at 460°C
AM0	0.911	0.828	0.913	0.888	0.941	0.924
AM2	0.892	0.813	0.895	0.866	0.915	0.898

Table 4.4 Emittance Values of Black Chrome Films in the As-Deposited Condition (Measured at 80°C)

Sample Number	ε	Sample Number	ε
Substrate	0.055	29Ba	0.092
19C	0.099	29C	0.098
19F	0.117	29D	0.131
20A	0.109	29E	0.108
20B	0.10	29F	0.118
20C	0.10	29J	0.121
20D	0.10	37A	0.128
21A	0.088	37B	0.092
21B	0.069	37C	0.095
21C	0.065	37D	0.095
22A	0.067	37E	0.111
22B	0.067	37F	0.098
		37Q	0.173

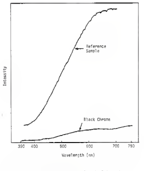

Figure 4 20a Typical intensity versus wavelength plot in the range of 350 ~ 750 nm (Black chrome film is 378 after 4 h at 460°C)

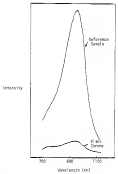

Figure 4 20b Typical intensity versys wavelength plots in the range of 700 - 1150 nm. (Black chrome film is 378 after 4 h at 460°C.)

at 1100 nm. This in turn leads to a greater error range at 1100 nm than at 900 nm (Figure 4.5). In the case of the PbS detector, the uncertainty results from the smallest reading on the ohmmeter. This value is already incorporated into the ≤ 10% dark noise value mentioned above. However, Pettit and Mahoney[36] observed that the highest accuracy possible with PbS detectors was ± 15%. This will be considered as the best error range possible with the PbS detector (1100 - 2500 nm).

c) Change in reflectance of the reference sample and the white coating of the integrating sphere. The values listed in Table 4.1 for true reflectance versus wavelength of the white coating indicate that at wavelengths ≥ 1900 nm, the true reflectance drops down to ≤ 80%. This reduces the intensity of the light reaching the detector, further increasing uncertainty in measurement.

d) Change in intensity of the light source. The W-halogen light source does not have constant light output over the entire wavelength range, typical relative output intensity is plotted in Figure 4.21. The figure shows that below 600 nm and above 1600 nm the relative intensity is very low. This, coupled with the other causes for uncertainty, increases the size of the error bars, particularly at higher wavelengths.

The error bars shown in the reflectance curve for the nickel substrate (Figure 4.5) are the result of the factors discussed above. As evident from the plot, they become uncomfortably large beyond about 1800 nm. The readings beyond this wavelength are, therefore, suspect

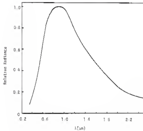

Figure 4.21 Relative radiance of a W-halogen lamp source as a function of wavelength.

For this reason, the reflectance curves for the various black chrome films are plotted out to about 2000 nm only, although it is expected that these curves could be extended to 2500 nm with reasonable confidence.

Solar Absorptance (α_s)

The value of solar absorptance calculated from the reflectance curves depends not only on the reflectance, but also on the solar energy spectrum chose, i.e., AM0, AM1, etc. This is because α_s incorporates both the wavelength-dependent absorptance and the spectral irradiance of the solar energy spectrum chosen, since different solar energy spectra have different spectral irradiance (Figure 1.1), the value of α_s also depends on the spectrum chosen. There is at present no standard solar irradiance specified. The approach suggested by ASTM[100] is to use the specific solar irradiant spectrum that best meets one's requirements, even if it is a local non-standard spectrum. This, of course, requires that the solar energy spectrum used should be reported along with α_s values. Unfortunately, most published values rarely specify the solar energy spectrum used. It is believed that most used AM1.5, this spectrum has itself not been standardized.[101] This suggests that comparison of α_s values is not necessarily reliable and that the better method is to compare reflectance curves. Furthermore, the single value of α_s does not indicate how wavelength specifically affects the absorptance. Most of the discussion here will therefore involve the reflectance curves, plotted in Figures 4.5 - 4.18.

A selected few of the reflectance curves are converted to α_s values to show typical values and changes (Table 4.3). The method used, explained below, is based on equation (1 2), given in Chapter I Using Kirchoff's relationship

$$\alpha_s + \tau_s + \ell_s = 1 \tag{4 2}$$

where α_s is the solar absorptance, τ_s the solar transmittance and ℓ_s the solar reflectance. Since, for opaque bodies, $\tau_s = 0$,

$$\alpha_s = 1 - \ell_s \tag{4 3}$$

The solar reflectance is obtained from

$$\ell_s = \frac{\sum_{i=1}^{n} \ell(\lambda_i) E_{\lambda_i} \Delta\lambda_i}{\sum_{i=1}^{n} E_{\lambda_i} \Delta\lambda_i} \tag{4 4}$$

where

E_{λ_i} = solar irradiance centered at λ_i over a width $\Delta\lambda_i$

$\Delta\lambda_i = \dfrac{\Delta\lambda_{i+1} - \Delta\lambda_{i-1}}{2}$

ℓ_{λ_i} = reflectance at λ_i

Equation (4.4) is a practical counterpart of equation (1 2) In equation (4 4), the value of E_{λ_i} depends on the solar spectrum chosen. Table 4 3 lists selected α_s values calculated using the AM0 and AM2 spectra, respectively The values of E_{λ_i} for the AM0 spectrum were obtained from the ASTM standards[102] while E_{λ_i} values for the AM2 spectrum were obtained from Figure 1.1. The values listed in Table 4 3 show that α_s values calculated with the AM0 spectrum are consistently higher than those with AM2. For example, as-deposited film 37Q has α_s of 0.941 when calculated with AM0 but only 0.915 when calculated with AM2.

Emissivity Measurements

The measured values of emissivities of as-deposited samples are listed in Table 4.4. The values range from a low of 0.066 for the bare nickel substrate to a high of 0.173 for coating 37Q. As reported by Pettit and Mahoney,[96] the accuracy of the emissivity value as measured with the AE emissometer was better than ± 0.03 emissivity units.

Discussion

The results plotted in Figures 4.6 - 4.19 and listed in Table 4.3 show that the reflectance (and hence the absorptance) is sensitive to both the deposition conditions and thermal exposure. Most samples showed increased reflectance with increasing thermal exposure time at a specific temperature. However, the extent of increase varied from sample to sample. Coatings such as 37Q showed little sensitivity to thermal exposure, whereas coatings such as 20C showed large increases in reflectance with thermal exposure. This suggests that the deposition conditions for 37Q were more conducive to thermal stability. The correlations between deposition conditions, thermal exposure, optical properties and composition will be discussed in more detail in Chapter VII. In general, the reflectance values increased when the oxide content was either below ~ 40 vol.% or above ~ 75 vol.%. The amount of oxide in the film, as will be shown later, was related to the deposition conditions as well as to the temperature of thermal exposure (and to a lesser extent, time). The deposition conditions affected the composition (and structure) of the as-deposited film. These, in turn, affected the extent of oxidation that occurred with thermal exposure.

The thermal emittance of the black chrome film is greater than that of the bare nickel substrate (Table 4.4). However, ε also varies as a function of the black chrome film deposition conditions. Black chrome films 21A - 22B, which are very thin and contain very little oxide (Chapter V), have emittance values very close to that of the bare nickel substrate. In general, the thermal emittance of thicker black chrome films (as measured from Auger sputter data) was higher than that of the thinner films. The changes in emittance of the as-deposited films will be discussed in more detail in Chapter VII.

CHAPTER V
ANALYSIS OF BLACK CHROME FILMS

Introduction

Black chrome films are a composite of chromium metal, chromium oxide(s), voids and possibly other compounds. The amounts of each may also not necessarily remain constant throughout the film. Therefore, to understand the behavior of these solar absorber films vis-a-vis their optical properties and thermal stability, it is necessary to determine the constituents in the film and their distribution.

The techniques used here include X-ray photoelectron spectroscopy (XPS), Auger electron spectroscopy (AES), secondary ion mass spectrometry (SIMS) and scanning electron microscopy (SEM)[103-105]. In addition, thermal desorption studies were also used to determine the presence of hydrated- and chlorine-containing species.

Experimental Procedure

XPS results were obtained using a PHI model 548 spectrometer in a pulse counting mode using a magnesium anode operated at 400 watts. The analyzer was a double cylindrical mirror with retarding grids. A pass energy of 25 eV (corresponding to a resolution of 0.3 eV) was used. Argon ions of 5 keV energy were used for sputtering. To avoid effects due to charging, the energy position of the oxygen 1s peak was used as a reference for aligning the chromium 2p photoelectron peaks.

AES was accomplished in a single pass non-scanning Perkin Elmer Corporation thin film analyzer using a primary beam energy of 3 keV, beam current of ~ 30 μA with peak-to-peak modulation voltage of 5 eV Argon ions of 2 keV energy were used for sputter depth profiling using a PHI ion gun The residual pressure was ≤ 5 x 10^{-8} Torr During sputtering, the system was backfilled with pure argon to a pressure of 4 x 10^{-5} Torr.

Thermal desorption and SIMS studies were done in a vacuum system where the residual pressure was ≤ 5 x 10^{-8} Torr. A modified UTI model 300C quadrupole residual gas analyzer was used, SIMS was done using a 3M model 30C system

SEM photomicrographs were obtained with a JEOL JSM 35C microscope operated at 25 kV accelerating voltage, sample working distance of 15 cm without sample tilt. Some films were examined in the as-deposited conditions, others after sputtering (i e , after Auger sputter depth profiling) and still others after scraping the film onto glass slides

Thermal aging tests were done in air in a tube furnace at the specified temperatures and for the specified times. Temperature control was better than ± 10°C.

Results

The results presented below include analysis of two sets of black chrome films The first involves black chrome films deposited under the conditions listed in Table 3 1, while the second involves films deposited at Sandia National Laboratories, Albuquerque, New Mexico. The second group of samples (from Sandia) were electrodeposited from the same type of bath and under similar conditions as those shown in Table 3.1. Long term thermal aging of these samples was done at Sandia, while short term thermal exposures (< 200 h) were done in the same tube furnace used for the first group of black chrome films (Table 3.1).

XPS Results

Data showed that the surface was always contaminated with carbon and sulfur, while Cl, Ca, K, Na, Fe and Si were observed occasionally. All these elements were essentially restricted to the surface. XPS results showed that the outer surface of the films was Cr_2O_3, as evident from Figure 5.1. The positions of the Cr $2p^{1/2}$ and $2p^{3/2}$ photoelectron peaks were determined from both a bulk Cr_2O_3 sample and a Cr film which had been oxidized at 300°C. The same peaks for metallic Cr were determined from a sputter cleaned Cr film. The photoelectron peaks from the 300°C film and sputter cleaned Cr are shown in Figure 5.2. It should be noted that there is a 1.9 eV shift between the $2p^{3/2}$ peak in metallic Cr compared to the same peak in Cr_2O_3. In addition, it should be noted from Figure 5.1 that the O 1s peak from the unsputtered surface has a high energy shoulder, indicative of the presence of a hydroxide on the surface.[106] However, the shoulder (i.e., the hydroxide) was quickly removed by sputtering, indicating that it only exists as a thin surface layer. SIMS data did not clearly confirm the presence of hydroxide in these films, although some authors have reported the presence of hydroxide in similar films.[31,40] Their films were deposited from standard Chromonyx baths but at current densities much higher (~ 269 mA/cm^2) and for shorter times (~ 1.5 minutes).

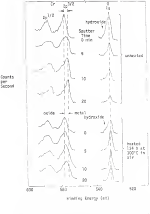

Figure 5.1 Cr 2p and O 1s XPS data as a function of sputtering time with 5 keV argon ions. Data are shown from both a black chrome sample which has not been heated and a sample exposed for 134 h at 300°C in air

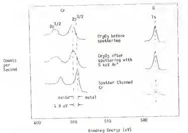

Figure 5.2 Cr 2p and O 1s XPS data from sputter cleaned chromium and from sputtered Cr_2O_3 films. The Cr $2p^{3/2}$ photoelectron line from Cr_2O_3 is broadened by sputtering because of reduction of Cr_2O_3 to Cr at the surface.

To determine the amount of Cr_2O_3 distributed throughout the film, the influence of sputtering on the Cr_2O_3 spectrum must be determined. XPS data in Figure 5.2 from Cr_2O_3 suggest that the 5 keV Ar^+ ion bombardment reduced some surface Cr_2O_3 to the elemental state. The sputter reduction of Cr_2O_3 can be accounted for by taking correction factors from the standards and subtracting peak intensities (based on these factors) from the observed total peak intensity. Ignatiev et al.[31] reported that the amount of chromium reduced from Cr_2O_3 increased with time. A time dependence for sputter reduction is normally observed only at very short times,[107] the sputter reduction of Cr_2O_3 in this study was constant after sputtering the Cr_2O_3 standard for ~ 1 minute. It is, therefore, assumed to be constant for mixtures of Cr and Cr_2O_3.

The XPS sputter profiles can be used to calculate the oxide content in the film. The values of the oxide and metallic chromium content were determined by integrating the areas under the sputter profiles for Cr^0 and Cr^{+3} and by normalizing the signal intensities to those obtained from pure Cr and Cr_2O_3. It was assumed that the densities of Cr and Cr_2O_3 in the black chrome films were equal to their bulk values. The volume fraction of oxide determined by XPS compares favorably with that calculated from AES sputter profile data (± 10%). Since AES data were more easily obtainable, oxide contents were generally obtained in this manner.

AES Results

Auger data showed that the surface was always contaminated with C, while Cl and S were frequently observed. These contaminants largely disappeared after sputtering for less than 1 minute ($\leq$ 50 Å), indicating that they were concentrated on the surface. A typical AES spectrum from the surface of a black chrome film is shown in Figure 5.3a. In addition to Cr and O, C, S and Cl are also evident. However, two minutes of sputtering resulted in the removal of S and Cl and drastic reduction in the carbon AES peak, this spectrum is shown in Figure 5.3b. A few of the black chrome films, electrodeposited under conditions listed in Chapter III, showed the presence of chlorine throughout the film. This is demonstrated by data in Figure 5.4a, which is an Auger sputter profile through sample 20C. Thermal exposure for 46 h at 460°C caused all the chlorine to be removed, as is evident from the Auger sputter profile after thermal exposure (Figure 5.4b). This feature was observed for all the films that showed Cl in the as-deposited film. Even a short thermal exposure (~ 1 h at 460°C) caused almost complete removal of Cl from the film. Thermal desorption studies, presented later in this chapter, were used to determine the temperature dependence of Cl removal.

As mentioned earlier, most of the black chrome films were not contaminated by Cl. Figures 5.5a and 5.5b are more typical for the deposited films. A sputter profile of a film in the as-deposited condition is shown in Figure 5.5a, whereas Figure 5.5b demonstrates the effect of 4 h thermal exposure at 460°C upon the composition. Note the increase in the oxygen peak height (relative to chromium) after thermal exposure; this is indicative of increased oxide content in the film.

Black chrome films 21A, 21B, 21C, 22A and 22B (Table 3.1) were noticeably different from the other films. Not only was their appearance grayish-white (instead of the near-black of the others), but the films were much thinner and contained much less oxide. This is demonstrated in Figures 5.6a - 5.6e, Figures 5.6a - 5.6d are Auger spectra of the

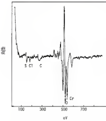

Figure 5.3a AES spectra of the surface of black chrome film 37B.

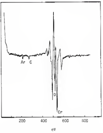

Figure 5 3b AES spectra of black chrome film 378 after sputtering for 2 minutes.

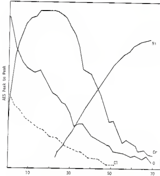

Figure 5.4a Auger sputter profile of sample 20C in the as-deposited condition.

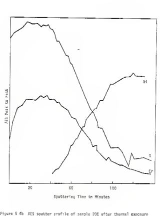

Figure 5 4b AES sputter profile of sample 20C after thermal exposure of 45 h at 460°C

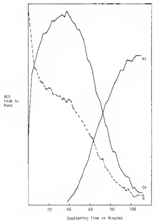

Figure 5-5a AES sputter profile of as-deposited sample 37B

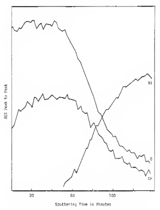

Figure 5.5b AES sputter profile of sample 378 after 4 h at 460°C

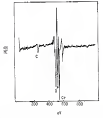

Figure 5.6a AES spectra of the surface of black chrome film 218

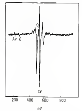

Figure 5.6b AES spectra of black chrome film 21B after 4 minutes of sputtering.

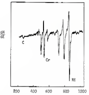

Figure 5.6c AES spectra of black chrome film 21H after 8 minutes of sputtering.

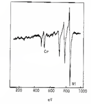

Figure 5.6d AES spectra of black chrome film 218 after 11 minutes of sputtering.

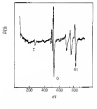

Figure 5.6e AES spectra of the surface of black chrome film 21B after thermal exposure of 26 h at 460°C

as-deposited film after different sputter times, while Figure 5.6e is the Auger spectra of the surface of the same film after thermal exposure for 26 h at 460°C. The data show that the as-deposited film was much thinner (≤ 200 Å) than the other, more typical, black chrome films (≥ 2000 Å). Furthermore, the amount of oxide in the films was very low, as is evident from the small O AES peak (relative to Cr). The data presented in Figure 5.6e showed that the thermal exposure of 26 h at 460°C caused all the Cr to be removed, most probably by flaking. The AES profile of the surface showed only nickel, oxygen and a small carbon peak. Visually, there was evidence of flaking on the thermally exposed films. This behavior was typical of all the black chrome films (21A - 22B), which had the greyish-white appearance.

The extent of oxidation in the black chrome films can be measured from the sputter profiles plotted in Figures 4 and 5. The percentage, $f_{Cr_2O_3}$, of chromium as Cr_2O_3 can be determined by integrating the areas under the sputter profiles and using the formula

$$f_{Cr_2O_3} = \frac{A_0 R}{(A_{Cr} - A_0 R)\,M + A_0 R} \times 100 \qquad (5.1)$$

where A_0 and A_{Cr} are the areas under the oxygen and chromium sputter profiles, R (≈ 0.46) is the ratio of chromium-to-oxygen Auger peak heights in a Cr_2O_3 standard and M ($= 0.37$) is the ratio of the chromium peak height in Cr_2O_3 standard to that in pure chromium. The derivation of equation (5.1) and the assumptions used are presented in Appendix D.

The volume fractions of chromium oxide in some of the films are listed in Table 5.1. These were calculated using equation (5.1). The percentages of oxide were observed to vary not only with deposition

Table 5.1 Volume Fraction Cr_2O_3 in Black Chrome Films as a Function of Deposition Conditions and Thermal Exposure

#	Thermal Exposure	Vol. Fraction Cr_2O_3
19F	as-deposited	0.48
	26 hr at 460°C	0.97
20C	as-deposited	0.50
	45 h at 460°C	0.94
	240 h at 396°C	0.91
29Ba	as-deposited	0.46
	26 h at 460°C	0.98
29C	as-deposited	0.46
	26 h at 460°C	0.92
37A	as-deposited	0.50
	27 h at 395°C	0.86
	4 h at 460°C	0.81
	67 h at 460°C	0.97
37B	as-deposited	0.53
	1 h at 460°C	0.87
	4 h at 460°C	0.91
	50 h at 460°C	0.92
	67 h at 460°C	0.96
37D	as-deposited	0.42
	27 h at 395°C	0.76
37F	as-deposited	0.37
37Q	as-deposited	0.33
	4 h at 460°C	0.65
	50 h at 460°C	0.79

conditions, but also with thermal exposure. The data show that all the films, irrespective of the deposition conditions, experienced a rapid increase in oxide content after only a few hours of thermal exposure. To demonstrate the effect of exposure time, the oxide content is plotted against exposure time at 460°C in Figures 5.7a and 5.7b. The oxide content is plotted linearly in time in Figure 5.7a, while Figure 5.7b is a logarithmic time plot. The latter clearly shows the logarithmic oxidation behavior of black chrome films electrodeposited from the Chromonyx bath.

To determine if the black chrome films obtained from Sandia National Laboratories exhibited similar oxidation behavior, they were subjected to similar thermal exposure treatments and the oxidation behavior determined; typical behavior is plotted in Figure 5.8. The behavior is identical to that of the black chrome films electrodeposited under conditions listed in Table 3.1 (Chapter III), i.e., rapid initial oxidation followed by increasingly slower oxidation.

To correlate the oxidation behavior of black chrome films with that of pure chromium, the oxidation of both bulk Cr and pure, metallic Cr films were studied, the details are given in Chapter VI. The results indicate that the mechanically polished bulk Cr samples had an oxidation behavior that was similar to that observed in black chrome. The electrodeposited Cr and Cr films, however, showed faster oxidation.

Thermal Desorption Results

The Auger data showed that some of the as-deposited black chrome films contained Cl throughout the film. However, Cl was removed from

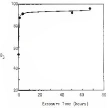

Figure 5 7a Variation of Cr_2O_3 content in black chrome film 37B as a function of exposure time at 460°C.

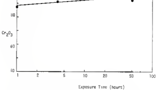

Figure 5 7b Variation of Cr_2O_3 content in black chrome film 378 as a function of exposure time at 460°C.

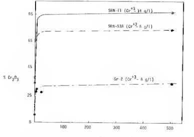

Figure 5.8 Variation of oxide content with exposure time at 395°C of black chrome films obtained from Sandia National Laboratories.

the films even after ~ 1 h at 400°C thermal exposure. To determine how and at what temperature Cl was desorbed, the black chrome films containing Cl were heated in vacuum and the desorbed species monitored. The desorption of atomic mass unit 36, corresponding to HCl^+, is plotted in Figure 5.9 as a function of temperature. Desorption was evident even at ~ 200°C, each time the temperature was raised (by increasing heating current), there was a sharp increase in the desorption of AMU 36. Time to heat the sample up to ~ 560°C was ~ 21 minutes, while the cooling period to ~ 50°C took almost 11 minutes. The results plotted in Figure 5.9 clearly show the sensitivity of Cl in the black chrome film to thermal exposure.

To determine if any water was also desorbed, AMU 18 was monitored. There was a small increase in the AMU 18 peak at temperatures ≥ 380°C while cooling the sample from ~ 600°C caused gradual decrease in the peak height). However, this increase in desorption of water could not be definitely ascribed to the black chrome film. Repeated experiments, with and without the sample, showed insufficient change in the peak height. The relatively large sample holder made determination of whether any of the desorbed water was from the black chrome sample difficult.

Desorption of H also showed a sharp increase in the same temperature range as that of water. However, as for water, attributing any of the desorbed H to the black chrome was difficult.

SEM Photomicrographs

Typical scanning electron photomicrographs are shown in Figures 5.10 - 5.13. Figures 5.10 and 5.11 are of the surface of black chrome film 20C in the as-deposited and thermally exposed conditions, respectively.

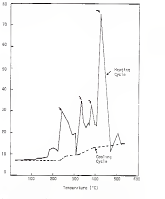

Figure 5.9 Thermal desorption of AMU 36 peak from black chrome film 20C as a function of temperature. The arrows represent the sharp increase noted as soon as heating current was increased by 1A (initial heating current was 2A)

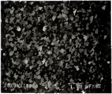

Figure 5.10 SEM micrograph of the surface of black chrome film 20C

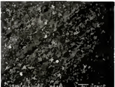

Figure 5.11 SEM micrograph of the surface of black chrome film 20C after thermal exposure of 45 h at 460°C

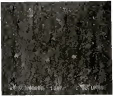

Figure 6.12 SEM micrograph of the surface of black chrome film 15C

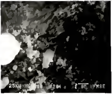

Figure 5.13 SEM micrograph of the scraped film fragments of a sur chrome film 37Q

Note that thermal exposure causes little or no change in agglomerate size. Figure 5.12 shows the surface of another as-deposited film while Figure 5.13 is a photomicrograph of film fragments (of film 37Q) scraped onto a glass slide. The SEM photomicrographs show that variation in agglomerate size within a film is relatively small, while variation from film to film is more significant. For example, film 20C had mean agglomerate size of ≤ 700 Å, while film 37Q had a mean agglomerate size of ≥ 1000 Å.

Effect of Oxide Content on Optical Properties

The relationship between the oxide content in the black chrome films and the hemispherical solar absorptance (α_s) and thermal emittance (ε) were obtained by comparing results presented in Chapter IV (Table 4.3 and Figures 4.6–4.10), this chapter (Table 5.1) and measured values of oxide content and optical properties on the black chrome films obtained from Sandia National Laboratories. The effect of the oxide content on α_s and ε are plotted in Figures 5.14 and 5.15, respectively. It can be seen that α_s remained nearly constant, and at its highest value, when the oxide content in the film was controlled between 40 ~ 75%. In the same oxide content range ε decreased linearly with increasing oxide content. Thus, to ensure that α_s did not significantly change during service, the oxide content in the film must be maintained within the range of 40 ~ 75%. Oxide contents ≤ 40% and ≥ 75% resulted in a sharp decrease in α_s. In comparing the oxide contents listed in Table 5.1, it is evident that all the black chrome films that had ≥ 45% of oxide in the as-deposited condition rapidly increased their oxide content on thermal exposure to ≥ 90%. This means

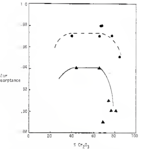

Figure 5.14 Variation of solar absorptance with Cr_2O_3 content in black chrome coatings
— 16 g/l Cr^{+3} bath, sulfamate Ni substrate
--- 8 g/l Cr^{+3} bath, sulfamate Ni substrate

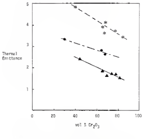

Figure 5.15 Variation of thermal emittance at 300°C with Cr_2O_3 content in black chrome coatings
— 16 g/l Cr^{+3} bath, sulfamate Ni substrate
—·— 8 g/l Cr^{+3} bath, 302 stainless steel substrate
--- 8 g/l Cr^{+3} bath, sulfamate Ni substrate

lower α_s, i.e., increased reflectance. A comparison of the reflectance curves (Figures 4.5 - 4.10) support this. As-deposited films, such as 37Q, which had ~ 33% oxide showed only slight changes in their reflectance since thermal exposure did not increase their oxide content beyond ~ 75%. In contrast, black chrome film GR2, obtained from Sandia National Laboratories, remained gray colored even after thermal exposure. This is because oxide content of this film was $\leq$ 30% even after thermal exposure (see Figure 5.8), this value is below the optimum range of 40 ~ 75%.

Summary of Results

The major results (presented above) can be summarized as follows.

1) XPS data identified the oxide present in the black chrome films to be Cr_2O_3. This is true for both the films electrodeposited according to the conditions listed in Table 3.1 (Chapter III) and those obtained from Sandia National Laboratories.
2) Minor constituents, such as C, Cl and S were mainly concentrated at the surface. A few of the black chrome samples had Cl present throughout the films.
3) The Cl present in some of the black chrome films was very sensitive to thermal exposure. Even 1 h at 400°C caused near-total Cl desorption. Thermal desorption studies showed that it was desorbed primarily as AMU 36 (i.e., HCl species).
4) The oxidation behavior of the black chrome films was logarithmic in nature, i.e., rapid oxidation during the early stages of thermal exposure followed by increasingly slower oxidation. This is similar to behavior observed on mechanically polished bulk Cr

5) The oxide content in the films, both in the as-deposited and thermally exposed condition, was dependent on the deposition conditions.

6) Black chrome films 21A through 22B were significantly different from the other films. They had a grayish-white appearance, very low oxide content and were very thin. Thermal exposure caused the film to delaminate from the substrate.

7) Scanning electron micrographs showed that the agglomerate size is related to deposition conditions. The size does not significantly change with thermal exposure, nor does it vary much within each individual film.

8) Solar absorptance remained constant and at its highest value when the oxide content in the black was between 40 - 75 vol %. At lower and higher oxide contents, α_s decreases rapidly. In the optimum oxide content range, ε decreases linearly with increasing oxide volume.

CHAPTER VI
OXIDATION OF PURE CHROMIUM

Introduction

The oxidation behavior of pure chromium is important in this study on black chrome films. The black chrome films exhibited a logarithmic oxidation behavior when thermally exposed in air at temperatures of 380 ~ 470°C. It is of interest to correlate this behavior with that of pure chromium. Although the oxidation behavior of pure chromium has been studied many times, most of the studies have been restricted to initial oxygen intake on clean surfaces[108-111] or thick oxide formation at temperatures greater than 700°C.[112-117] Furthermore, the majority of these investigators studied chromium oxidation in pure oxygen, typically at less than 1 atmosphere. In the lower temperature studies times of less than 2 h were typically used.[108,109,113] Use of pure oxygen avoids the simultaneous interaction of the metal surface with constituents of air, such as nitrogen and water vapor, which may produce synergistic effects during oxidation.[118]

This study focusses on the oxidation of pure chromium, in the temperature range of 270 - 490°C in air atmospheres for exposures from 1 h to more than 100 h. This is because black chrome films are subject to such conditions and the use of air is to compare the oxidation behavior of pure chromium and black chrome under similar conditions.

Experimental Procedure

The chromium samples were in the form of electrodeposited nodules obtained from A. O. McKay. Emission spectrographic analysis gave the following results: [Fe], [Mg] and [Ni] < 0.01% each, while B, Sb, As, Mn, Pb, Si, N, Ge, Bi, Cd, Be, In, Sn, Mo, V, Cu, Ag, Zn, Zr, Tl, Co, Cd, Sr, Ca and Al were not detected. Samples were mechanically ground and polished through a series of grits. The final grinding stage was with wet SiC paper, while the last two polishing stages used diamond paste of particle sizes 6 μm and 1 μm, respectively. Polished samples were ultrasonically cleaned with Alconox detergent and water, thoroughly washed with deionized water and dried with methanol. One sample for each time-temperature combination was thermally aged in a tube furnace in air at temperatures between 270 and 490°C. Temperature control was better than ± 5°C.

To test the effect of surface preparation on the oxidation rate, some of the polished samples were subsequently electropolished in a 5 vol.% solution of perchloric acid in CH_3COOH at 14 - 16°C. Polishing was incremental in 10 - 15 s bursts at approximately 0.4 A/cm^2, for a total time of 100 - 150 s. These samples were thermally oxidized at 390°C. Pure chromium films 1400 Å thick, vapor deposited onto sodium borosilicate glass substrates, were also oxidized at temperatures ranging from 320 to 490°C.

Oxidized samples were analyzed for surface composition and oxide thickness by AES. The details of the procedure are given in Chapter V. The sputter rate for chromium oxide was determined by measuring the sputtered depth after various bombardment times on oxidized films or on a bulk Cr_2O_3 sample. Sputtered depths were measured with a Sloan Angstrometer or a Sloan Dektak profilometer. To account for day-to-day variations in the sputter rate, a standard thickness of chromium on glass was used as a sputter rate standard.

Results

A typical AES spectrum from an oxidized sample is shown in Figure 6.1a. The oxide surface was always contaminated with C and frequently contaminated with S and Cl. These contaminants largely disappeared in less than 1 minute of ion sputtering (corresponding to ≤ 50 Å), indicating that they were concentrated on the surface. This is demonstrated in the AES spectrum (Figure 6.1b) taken after 2 minutes of ion sputtering. The oxide formed on chromium under these conditions has previously been shown to be Cr_2O_3 [108,109,118]. No evidence of chromium nitride was observed.

Typical sputter depth profiles for two oxidized chromium samples are shown in Figure 6.2. It should be noted that the zero levels are shifted in Figure 6.2 to show more clearly the difference in oxide thicknesses. Oxide thicknesses were calculated by measuring the sputtering time required to reduce the oxygen peak-to-peak height to half its maximum value and multiplying by the sputter rate previously determined for Cr_2O_3 (~ 80 Å/min).

The oxide thickness on mechanically polished samples exposed only to room temperature without any thermal treatment was determined to be 58 ± 15 Å. The variation in oxide thickness on mechanically polished samples as a function of time at different temperatures is plotted on a semilogarithmic scale in Figure 6.3. The oxide thickness increased as both time and temperature increased.

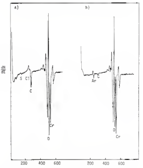

Figure 6.1 Auger spectra of mechanically polished Cr samples a) surface, b) after two minutes of sputtering with Ar^+ ions at 4×10^{-5} Torr pressure.

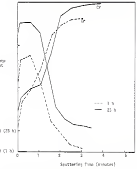

Figure 6 2 Auger sputter profiles of mechanically polished Cr thermally exposed at 270°C for 1 h and 23 h [The zero level for the 23 h profile has been shifted as indicated]

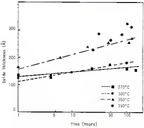

Figure 6 3a Variation of the oxide thickness on mechanically polished Cr as a function of time at different temperatures

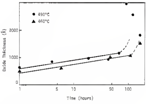

Figure 6 3b Variation in the oxide thickness on mechanically polished Cr as a function of time at different temperatures.

The effect of surface preparation on the oxidation behavior is shown in Figure 6.4, which is a plot of the oxide thickness as a function of time at 390°C for mechanically polished and electropolished samples. The electropolished samples had larger oxide thicknesses than the mechanically polished samples.

Oxide thicknesses for chromium films on glass and for bulk chromium are compared in Table 6.1. The oxide thicknesses on the chromium films were obtained by heating in the temperature range 320 - 490°C for various times, while the oxide thicknesses on bulk chromium were obtained by interpolation from the plots in Figure 6.3. The table shows that the Cr films oxidized completely in ≤ 44 h at 490°C, the Cr film thickness was ~ 1400 Å. The table also shows that the Cr film oxidized much more rapidly than the bulk Cr specimens.

Discussion

The results show that on mechanically polished Cr samples the oxide thickness increased with increasing time and temperature, but at a slower rate than that on the electropolished bulk Cr or for Cr thin film samples. The as-polished oxide thickness on bulk Cr, determined to be 58 Å, is larger than the reported value of about 20 Å.[108,109] The higher oxide thickness is probably a result of mechanical polishing effects since the previously reported values are for electropolished and thin Cr films. Although the as-electropolished oxide thickness was not accurately measured, it was less than that of the samples as-mechanically polished

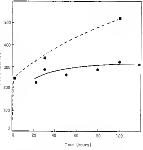

Figure 6-4 Effect of surface preparation on the oxide thickness versus aging time at 390°C.
--- electropolished Cr
— mechanically polished Cr

Table 5.1 Comparison of Oxide Thicknesses on a 1400 Å Chromium Film on Glass and on Mechanically Polished Bulk Chromium After Thermal Aging

Thermal Aging	Oxide Thickness (Å)	
	Cr Film on Glass	Bulk Cr
320°C, 5 h	210	145
375°C, 23 h	702	240
490°C, 1 h	862	662
490°C, 4 h	fully oxidized	1075

The data obtained on the mechanically polished samples were fitted to several power law and logarithmic rate equations[108,112] and regression analysis was used to determine which of the following equations gave the best description of oxide thickness versus oxidation time

$$y = mt_0 + c \qquad \text{(linear equation)} \qquad (6.1)$$

$$y = mt_e^{1/2} + c \qquad \text{(parabolic equation)} \qquad (6.2)$$

$$y = mt_0^{1/3} + c \qquad \text{(cubic equation)} \qquad (6.3)$$

$$y = m\log(t_0 + 1) + c \qquad \text{(logarithmic equation)} \qquad (6.4)$$

$$\frac{1}{y} = m\log(t_e + 1) + c \qquad \text{(inverse logarithmic equation)} \qquad (6.5)$$

where y represents the oxide thickness in Angströms, t_0 the thermal aging time in hours, m the slope and c the intercept.

Regression analysis of oxide thickness versus time was performed using a Statistical Analysis Systems Institute software package[119] available on an Amdahl computer. A general linear model procedure was used. R^2 values as a function of temperature for each of the above equations are listed in Table 6.2. R^2 represents that proportion of the total variability of the y values that is accounted for by the independent variable t_0. It is a measure of the degree to which the data fit the equations under consideration; a value of unity implies perfect fit.[120,121] The value of the slope obtained from regression analysis for the logarithmic equation (equation (6.4)) was used to draw the oxide thickness versus time plots as a function of temperature in Figure 6.3. The table also lists the student t values and the probability for null hypothesis

Table 6.2 Regression Analysis Results for the Various Equations as a Function of Temperature

Equation	270°C			300°C			350°C		
	R^2	Values for slope, m		R^2	Values for slope, m		R^2	Values for slope, m	
		t*	PR†		t*	PR†		t*	PR†
linear $y=mt_0+c$	0.231	1.10	0.3341	0.868	4.44	0.0212	0.642	2.68	0.0654
parabolic $y=mt_0^{1/2}+c$	0.421	1.71	0.1631	0.968	9.50	0.0025	0.784	3.81	0.019
cubic $y=mt_0^{1/3}+c$	0.494	1.98	0.1191	0.987	15.30	0.0006	0.876	5.33	0.006
logarithmic $y=m\log(t_0+1)+c$	0.599	2.44	0.0708	0.989	16.73	0.0005	0.928	7.19	0.002
inverse logarithmic $\frac{1}{y}=-m\log(t_0+1)+c$	0.641	-2.67	0.0558	0.995	-25.17	0.0001	0.90	-6.0	0.0039

* t value is for H_0 (null hypothesis) parameter, m=0

† PR is the probability t > |t|

Table 6.2 (continued)

Equation	460°C			490°C		
	R^2	Values for slope, m		R^2	Values for slope, m	
		t*	PR†		t*	PR†
linear $y=mt_o+c$	0.790	2.75	0.1110	0.731	2.65	0.0649
parabolic $y=mt_o^{1/2}+c$	0.922	4.87	0.0397	0.803	3.50	0.0395
cubic $y=mt_o^{1/3}+c$	0.950	6.16	0.0253	0.827	3.79	0.0323
logarithmic $y=m\log(t_o+1)+c$	0.965	7.45	0.0175	0.842	4.0	0.0261
inverse logarithmic $\frac{1}{y}=m\log(t_o+1)+c$	0.976	-9.0	0.0121	0.833	-3.87	0.0306

* t value is for H_o (null hypothesis) parameter, m=0

† PR is the probability t < |t|

$(H_0 : m = 0)$ that $t > |t|$, $|t|$ is a value obtained from standard tables. In the null hypothesis $(H_0 : m = 0)$ it is hypothesized that the variable y is not related to the independent variable t_0[120,121] For the relationships listed above (equations (6.1 - 6.5)) to exist, it is necessary that the null hypothesis be rejected. For a smaller value of this probability, the confidence that the null hypothesis is rejected is greater.

The values in Table 6.2 indicate that a better fit was obtained with either the logarithmic or the inverse logarithmic equation. This is also shown in Figure 6.5, which is a plot of the oxide thickness at 350°C with the time scale varied in accord with the different equations (equations (6.1 - 6.4)). It is obvious from Figure 6.3b, however, that at 460°C and 490°C and long times ($t > 100$ h) the rate of oxidation increased dramatically. Although it is certain that the oxidation rates increased under these conditions, reliable thickness measurements were not possible because of spallation of the oxide. Spallation was visually observed on samples heated for more than 70 h at 490°C and on the sample heated for 165 h at 460°C. This tendency to spall has previously been reported by Lillerud and Kofstad[116] in association with logarithmic oxidation behavior.

The oxide thickness data plotted in Figures 6.3 - 6.5 were obtained from sputtered depth profiles such as those shown in Figure 6.2. Each datum represents the value obtained from a spot on a single Cr sample. The main causes for variability in the values plotted are variations in the as-polished surface condition of the sample, temperature variation (within the ± 5°C range) and sputter rate variation during Auger analysis. The thicknesses of the oxide determined at two different spots on the same mechanically polished Cr specimen heated for 50 h at 300°C were 173 and 185 Å

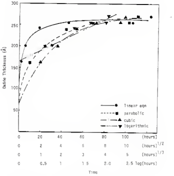

Figure 6.5 Plot of oxide thickness as a function of time at 350°C for the different equations ((6.1) - (6.4)).

Similarly, on a sample heated for 100 h at 390°C, the values were 317 and 323 Å. The oxide thicknesses obtained from two different mechanically polished Cr samples heated for 43 h at 490°C were 940 and 1056 Å. The precision of the analysis appeared to be good. However, the thickness of oxide on mechanically polished Cr samples heated at 390°C showed greater scatter in thickness than at other temperatures, particularly for aging times of 23 h or less. Thus, regression analysis results on the 390°C samples are not included. The data presented in Figure 6.4, however, show that distinct differences in oxidation rates were obtained for electropolished versus mechanically polished Cr at 390°C.

Fehlner and Mott[122] have suggested that the oxide thickness should increase logarithmically by diffusion occurring along grain boundaries in the presence of a concentration gradient. Grain boundaries are assumed to disappear with grain growth and crystallization (or recrystallization) of the oxide. Both Alessandrini and Brusic[109] and Lillerud and Kofstad[116,117] have reported grain growth in chromium oxide with increasing time at temperature. While the former reported parabolic oxidation behavior, the latter obtained an approximately logarithmic oxidation behavior. Lillerud and Kofstad concluded that grain growth gradually eliminated the easy diffusion paths available during initial oxidation, resulting in the logarithmic behavior. Others[115-117,123] have also suggested that the gradual blocking, deactivation or annealing of diffusion paths with time results in logarithmic oxidation rates. Evans[123] has suggested that voids may develop during oxidation which may reduce the area of the scale available for solid state transport, thus resulting in slower oxidation rates at longer times. Rhines and Connell[124] obtained a cubic growth rate on nickel. They explained this by suggesting that the new oxide formed along the grain boundaries, where oxygen diffusion inward along grain boundaries met nickel diffusing out through NiO grains.

While the present data are best described by a logarithmic equation, most published data on chromium oxidation at shorter times and higher temperatures have been reported to be consistent with a parabolic law.[108,109,112-115] A number of factors may lead to the operation of a different oxidation law in the present instance, including oxygen pressure and surface preparation effects. Most of the published results are for Cr samples subjected to thermal oxidation under partial vacuum and/or for times ranging up to only 2 h. The present data are from Cr samples that were thermally treated in air at atmospheric pressure for times ranging from 1 h to more than 100 h. However, both Fehlner and Mott[123] and Young and Cohen[125] have reported that the oxidation behavior of Cr was not sensitive to oxygen pressure at low temperatures (≤ 300°C). Young and Cohen also reported a negative exponent for the pressure term in the oxidation rate equation; its value became slightly more negative as the temperature was increased to the range of 400 - 600°C. Oxygen pressure, therefore, is unlikely to be a major reason for the logarithmic behavior.

Comparison of the present data with published results is also made difficult because of surface preparation effects. Most of the published data are for electropolished Cr samples, whereas this study deals mainly with mechanically polished samples. Two possible differences resulting from these different preparation procedures are surface roughness and surface purity. Kubaschewski and Hopkins[112] have reported that surface roughness may either increase or decrease the oxidation rate in metals, but they also argue that the rate would revert back to normal oxidation behavior as the oxide becomes thicker. An increased oxidation rate is easy to understand since a rough surface would have a high ratio of actual area to geometric area. Thus, the larger total surface area of a rough sample may lead to more rapid reactions. However, in some instances rough surfaces lead to slower reaction rates. The reasons for this are much less clear than those for the opposite case, but Kubaschewski and Hopkins also report that the oxide grain size is affected by surface roughness. It seems reasonable to speculate here that surface roughness, through its effects on oxide grain size, may lead to more rapid oxide recrystallization and a reduction of the easy diffusion paths discussed above. Under these circumstances, slower oxidation rates may be expected from rough surfaces. This may also cause the observation of logarithmic behavior in this instance, while parabolic oxidation dependence has been previously reported. The conclusion that roughness is important to the oxidation rate is reinforced by the fact that both the vapor-deposited and electropolished samples oxidized much more rapidly than mechanically polished samples. However, the time dependence of oxide thickness cannot be determined in the present instance for the two other surface preparation techniques because of limited data.

To ensure that the different behavior obtained for the mechanically polished and electropolished samples was not due to impurities introduced during processing, their Auger spectra were compared. In all cases (mechanically polished, electropolished and vapor deposited), the surface contaminants found were the same (i.e., S, C and Cl) and in approximately the same amounts. There were also no major differences in impurities in the bulk Cr samples.

The longer thermal aging time period (from 1 h to more than 100 h) of this study as compared to most published results (≤ 2 h) may also have been a factor in the different oxidation behavior. Although most published results[108,109,112-115] report a parabolic growth law, it is not clear whether their analyses were sufficiently rigorous to preclude the possibility that the growth equation was other than parabolic. The short time period (≤ 2 h) may also have led to an erroneous conclusion since it may have been insufficient to fully reveal the correct growth behavior.

While the present data is best fitted by a logarithmic equation, the regression analysis results are not definitive enough to completely preclude the possibility of fitting the data to another equation, such as cubic. The present investigation was conducted to determine if the oxidation of black chrome selective solar absorber coatings and pure bulk chromium metal were similar when exposed for long time periods in the temperature range of 270 - 490°C, the results demonstrate similar behavior.

CHAPTER VII
DISCUSSION OF EXPERIMENTAL RESULTS

A number of results were presented in the preceding chapters. In this chapter, their significance vis-a-vis each other will be discussed. First, however, the methods used for reduction of data presented in Chapter V (dealing with the analysis of black chrome films) will be discussed.

Data Reduction

The compositions of the black chrome films were obtained principally by XPS and AES (Chapter V). XPS analysis showed that the oxide present in these films was Cr_2O_3. This was determined from measurements of the drift in the $2p^{3/2}$ photoelectron peak and comparing with pure Cr_2O_3 and pure Cr, as explained in Chapter V. A number of other researchers have also reported the oxide to be Cr_2O_3,[12,31] although some have reported the presence of hydrated species.[40,41] The black chrome films analyzed in this study did not contain any hydrated species in the bulk of the films. Neither XPS data, such as shown in Figure 5.1, nor SIMS analysis indicated hydrated species. The only hydroxide observed by XPS was at the surface of the black chrome film, but sputtering for < 5 minutes resulted in complete removal.

XPS data, such as those shown in Figure 5.1, indicated that the surface of these black chrome films was entirely composed of Cr_2O_3. With increasing depth into the film, the amount of metallic Cr increased. This is demonstrated by the shift in the Cr $2p^{3/2}$ peak towards the metallic Cr binding energy with increasing depth into the film. The same trend was also predicted by Auger sputter depth profile data, such as shown in Figures 5.4 and 5.5, i.e., increased metallic Cr with increased depth into the film. Ignatiev et al.,[31] however, suggested that the increase in metallic Cr was not real but was an artifact of sputtering. They reported that oxygen in Cr_2O_3 was preferentially sputtered, the rate of this preferential sputtering increasing with time. Such behavior was not observed in this study. Sputter reduction of a Cr_2O_3 standard was observed, but was constant after sputtering for ~ 1 minute under conditions similar to those under which black chrome films were analyzed. This is shown in the XPS spectra in Figure 5.2. The Cr $2p^{3/2}$ photoelectron line from Cr_2O_3 broadened after ~ 1 minute of sputtering (indicative of some sputter reduction of Cr_2O_3 to Cr). Further sputtering did not cause any changes, i.e., sputter reduction was constant after ~ 1 minute. [Such short term time-dependent preferential sputtering has also been observed elsewhere.][107] It was, therefore, assumed that the black chrome preferential sputtering behavior was similar to that of pure Cr_2O_3, i.e., constant sputter reduction after ~ 1 minute (or a short time) of sputtering. This implies that observed changes in metallic Cr concentration as a function of depth into the film were not due to sputtering artifacts but due to real changes in composition. Because the time period during which preferential sputtering changes was so short compared to the total sputtering time (< 1%), only very small corrections would be necessary in any calculations based on sputter profile data of black chrome films.

Although film composition can be determined from XPS data, Auger sputter profile data (e.g., Figure 5.4) are more rapidly obtained. In addition, the results agree with XPS results within experimental error (± 10%), as shown in Chapter V. The oxide contents, listed in Table 5.1, were, therefore, calculated from the areas under the oxygen and chromium Auger sputter profiles using equation (5.1). The film substrate interface was determined as that point at which the Cr Auger signal decreased to half its maximum peak height. The area used for calculating $f_{Cr_2O_3}$ in equation (5.1) was assumed to be peak height times sputter time. Assuming that sputter time can be used rather than depth ignores the effect of differential sputtering rates, i.e., it assumes that the sputter rates for Cr and Cr_2O_3 are the same. This is not true. Metallic Cr was observed to sputter only half as quickly as Cr_2O_3. Therefore, the interface between Cr_2O_3 in the film and the substrate occurs after shorter sputtering times than for metallic Cr (in the film) and the substrate. This argument assumes that the sputter rates are not interfered with by the relative distributions of Cr and Cr_2O_3. Such an assumption is not entirely realistic for black chrome films since some interference must occur. For example, any Cr_2O_3 present just under a Cr particle cannot be sputtered unless the Cr particle has been sputtered away. It should be noted that increased interference would only shift the calculated oxide content (Table 5.1) closer to the true value. Thus, a system in which there is no interference represents the case where the error introduced due to non-consideration of differential sputtering is a maximum. The extreme cases of no interference and complete interference are illustrated by the hypothetical microstructures shown in Figure 7.1

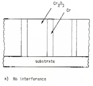

a) No interference

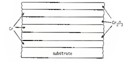

b) Complete interference

Figure 7.1 Hypothetical microstructures that exhibit extreme cases of interference with differential sputtering

The vertical columns of Cr and Cr_2O_3 in Figure 7.1a represent a film where differential sputtering would occur without interference, while the horizontally layered film, shown in Figure 7.1b, represents the case where there is complete interference. Note that the microstructure of black chrome films represents an intermediate case.

To determine the effect of differential sputtering in black chrome films, the change in volume fraction of Cr relative to ($Cr + Cr_2O_3$) as a function of depth into the film is plotted in Figure 7.2. The volume fractions were calculated from the relative peak heights of the Cr and O Auger signals and with equation (5.1). In the equation, the peak heights of Cr and O were used rather than areas. For the differential sputtering calculation, the O and Cr peak heights that correspond to the same point in the film occur at different sputter times. For example, the Cr metal content given by the Cr Auger signal after 40 minutes of sputtering and the Cr_2O_3 content given by the O Auger signal after 20 minutes of sputtering gave the composition of the same depth from the surface of the film. This is because Cr_2O_3 sputters twice as fast as Cr. Noting that the Cr Auger signal is a sum of the signal due to Cr metal and Cr_2O_3, the Cr Auger signal due to Cr metal is given by

$$I_{Cr} = I_C - I_O R \qquad (7.1)$$

where I_C is the total Cr Auger signal, I_O is the O Auger signal after the same sputtering time and R (= 0.46) is the same constant used in Chapter V.

The plots in Figure 7.2 show that differential sputtering causes a small change in the volume fraction of Cr, the change being negligible for the thermally exposed film. Thus, oxide content determinations that ignore the differential sputtering effects are not unreasonable.

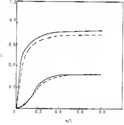

Figure 7.2 Variation of volume fraction Cr relative to ($Cr + Cr_2O_3$), given by Ω, as a function of depth in black chrome film 37Q
— no differential sputtering
--- with differential sputtering

Effect of Oxide Content on Optical Properties

Solar Absorptance

The solar absorptance of black chrome films was determined from reflectance curves, such as Figures 4.6 - 4.19. Typical values for the absorptance are listed in Table 4.3. In comparing these values with the oxide contents listed in Table 5.1 and plotted in Figure 5.19, it is clear that there is a direct correlation between the oxide content in the film and its solar absorptance. The main correlations are as follow

a) α_s exhibits a maximum when the Cr_2O_3 content in the thermally exposed films is between 40 and 75%

b) α_s is relatively constant at its maximum value when Cr_2O_3 is between 40 and 75%. Above and below this range, α_s decreased rapidly.

c) The maximum value of α_s is different for different films.

Therefore, to maintain the solar absorptance constant and at its maximum value during service, the Cr_2O_3 content must be maintained in the range 40 - 75%. It should be noted that changes in void volume and distribution can cause this range to shrink or expand. Voids are believed to play an important role in the thermal stability of these films as well. These effects are discussed in more detail later.

Changes in surface roughness of the black chrome film or the substrate have also been reported to cause changes in solar absorptance.[1,8,12,17,18,126] Pettit and Sowell reported a 5-6% increase in solar absorptance when deposited on rough substrates (1 - 2 μm scale irregularities), while Smith et al.[126] reported that the surface of the black chrome films was intrinsically rough (on a scale comparable to their thickness) and that the solar absorptance obtainable was dependent on this surface roughness. They also reported that this surface roughness decreased with increasing thermal exposure.

The surface of the nickel-plated steel substrate used in this study had a surface roughness comparable to the film thickness. The surface profile of the bare substrate is shown in Figure 3.1. The irregularities on the surface are 500 - 1500 Å, while the film thicknesses are ~ 2000 Å. Therefore, even if the film was smooth, the surface of the film would have a roughness profile similar to that shown in Figure 3.1. Black chrome films, electrodeposited from the Chromonyx type bath appear to have a uniformly rough profile largely independent of deposition conditions. This is reflected in the similar nature of their oxidation behavior--optical properties correlation, viz., relatively constant absorptance when the oxide content is in the range of 40 - 75%. A physical measurement of the actual surface roughness with the Dektak profilometer was not possible because the films are very friable. SEM photomicrographs showed no apparent changes in surface roughness. However, Smith et al [126] observed some changes in surface roughness with thermal exposure by using a non-contact stereo profilometer specifically devised for this purpose. Such changes would have only minor effects (~ 1%) on the values of solar absorptance.

The decrease in the solar absorptance at oxide contents greater than ~ 75% is due to the decrease in the number of multiple interactions of the solar irradiance with the composite film with increasing Cr_2O_3. The film acts more and more like a simple homogeneous film of Cr_2O_3. Therefore, changes in reflection become more dependent on changes in refractive index and the film thickness than on the multiple scattering by Cr particles within the film. The value of 75% oxide at which the solar absorptance decreased is not an absolute value, it can vary depending on the distribution and relative volumes of voids, agglomerates and agglomerate size. For films with uniformly distributed voids and constant agglomerate size, this variation is estimated to be ~ 5 vol % of oxide. This estimate is based on observed variations in the oxide content when deposited and thermally exposed under similar conditions. Non-uniform changes can, however, cause larger variations.

The decrease in the solar absorptance at low oxide content (< 40%) is a result of the more metallic nature of these films. The layer concentration of metallic Cr particles in these films results in more metallic behavior, i.e., more reflectance at the lower wavelengths. Films with ≤ 30% oxide are greyish in color due to the semi-metallic reflective nature of these films. The decrease in absorptance can also be related to changes in the voids. Low oxide content films appear to be more dense, i.e., contain lesser voids. The lower void volume changes the number of multiple interactions of solar irradiance with the film. Under these conditions of high metallic Cr content and low void volume, the film acts more like a dense metallic film than like a composite film of Cr particles dispersed in a matrix of Cr_2O_3 and air (voids). Therefore, there is increased reflectance.

It should be noted that high solar absorptance can be achieved with a combination of Cr particles dispersed in a medium of air. However, to achieve high absorptance with such a system, the Cr particles must be non-spherically shaped to ensure absorption by wavelength discrimination[1] rather than by the multiple scattering effect used in composite systems.

Thermal Emittance

The thermal emittance values measured for the as-deposited films are listed in Table 4.4. As expected, the bare nickel-plated steel substrata had the lowest emittance (0.055), while black chrome film 37Q had the highest (0.173). Thermal emittance of black chrome film has been reported to increase with increasing thickness of the film due to a shift in the absorption edge to longer wavelengths.[12] This was observed with the black chrome films studied. For example, films 29C and 29Ba had the same oxide content, but the thermal emittance of 29C was higher than that of 29Ba. This was because 29C was ~ 25% thicker. Similarly, the higher emittance of 37Q was due to its greater film thickness.

Films containing very high metallic Cr contents, such as 21A through 22B, have low thermal emittance values since they behave like metal films. Films containing more oxide, such as 37Q, show higher thermal emittance because of the multiple scattering (and entrapment) of the long wavelength thermal waves (~ 2 µm). However, with increased oxidation, the thermal emittance must decrease because of the decrease in the multiple scattering due to the decreased metallic Cr content.[18] This was indeed observed, as shown in the plots of Figure 5.19. They show that with increased oxide content in these films (during thermal exposure), the thermal emittance decreased linearly.

Prediction of Microstructure from Optical Properties

The solar absorptance and thermal emittance properties of the black chrome films are a direct result of the substrate used and the microstructure of the black chrome films. Therefore, prediction of the microstructure from the values of the solar absorptance and thermal emittance should be conceivable. However, this requires an unreasonable number of assumptions. Since the absorptance and emittance are single number values of the behavior of a black chrome film over different wavelength ranges (0 - 2 μm and 2 - 20 μm, respectively), prediction of the reflectance curves from these values requires assumptions about the microstructure. This would then predict how the reflectance curves would change with absorptance and emittance. But, as explained elsewhere in this chapter, changes in the microstructure occur with thermal exposure and with the deposition conditions. Therefore, although the optical properties can be estimated from model calculations based on the microstructure, the reverse is much more difficult and unreliable.

Oxidation Behavior of Black Chrome

Some of the features relating to the oxidation behavior of these films on thermal exposure have already been discussed. The oxidation of all the electrodeposited black chrome films show the same logarithmic behavior. This means that there is rapid oxidation within the first few hours of thermal exposure followed by increasingly slower oxidation. This type of behavior implies that the oxide formed during the initial stages of thermal exposure protects (or passivates) the Cr particles to slow subsequent oxidation. This is true despite the fact that the as-deposited films have ≥ 30% Cr_2O_3 in them.

The effect of a thin overlayer on the oxidation behavior of black chrome films was studied to determine if it caused any changes. The results of depositing a thin overlayer of SiO_2 are presented in Appendix E.

The SiO_2 layer simply acted as an additional passivating layer. It caused a reduction in the extent of oxidation with thermal exposure, probably by reducing the number of pores at the surface. This is evident from the results on the oxidation of black chrome films with and without the SiO_2 overlayer (Figure E.2). Overlayers of SiO_2 can thus be used for added protection or for selvaging black chrome films that were deposited under conditions that cause rapid degradation. The presence of an overlayer will affect the optical properties of the film. Pettit and Brinker[128] observed a decrease in the solar absorptance with sol gel coatings. However, proper match of the refractive indices could prevent any decrease in absorptance; an increase may also be possible.

The conclusions that can be drawn from the oxidation behavior of black chrome films are as follow

a) The as-deposited oxide provides only poor protection for the Cr particles from oxidation on thermal exposure.

b) The oxide formed during thermal exposure is the only protective coating

c) An overlayer (of SiO_2) reduces the extent of oxidation of Cr to Cr_2O_3 by acting as an additional protective layer.

A comparison of the increase in oxide content with thermal exposure of the different black chrome films shows no clear correlation between films. All the films show the same rapid initial increase in oxide content with thermal exposure. However, the increase in oxide content or the increase relative to the as-deposited oxide content do not follow any consistent pattern. This suggests that the change in composition in these films is associated with change in the morphology of the films. A comparison of the agglomerate size with the oxide content again shows no clear correlation. Thus, changes in the extent of oxidation are likely to be related to changes in the void volume (and distribution) and other effects, which will be discussed later in this chapter.

A comparison of the oxidation behavior of black chrome with pure Cr shows that its behavior is similar to that of mechanically polished Cr. Therefore, passive oxide thickness data for mechanically polished bulk Cr can be utilized to indicate the thickness of the passive oxide layer that must form on the Cr particles at any temperature-time combination. Furthermore, lifetime of the solar absorber can be predicted since changes in its optical properties are related to its oxide content. For example, data in Figure 6.3 indicate that a passive oxide layer of $\leq$ 325 Å would form on the Cr particles when thermally exposed for ~ 10,000 h at 350°C. The same film, thermally exposed for ~ 100 h at 460°C would produce a passive layer of > 800 Å. Noting that total Cr_2O_3 = As-Deposited Oxide + Passive Oxide, the minimum size of the Cr particles can be estimated (assuming uniform sized spheres) to ensure that the Cr_2O_3 content in the film does not exceed ~ 75% during service at any specific temperature. For example, black chrome films that increase their oxide content from 30 to 70% when thermally exposed for 10,000 h at 350°C would need to have Cr particles of ~ 700 Å in the as-deposited film. Note that because of the logarithmic character of oxidation, increasing the particle size to ~ 950 Å would give a lifetime of 100,000 h at 350°C. However, since oxidation rates increase exponentially with temperature, similar calculations indicate that the Cr particle size would have to be $\geq$ 2000 Å at 460°C for thermal stability after 10,000 h. The change in particle size and corresponding growth in oxide thickness is shown in

Figure 7.3. This assumes a 325 Å thick passive layer formed around each particle (at 350°C), this being the only passivating layer. The calculation also assumes that the density expansion from the metal to the oxide is 50% and is accommodated by an increased oxide layer thickness.

Stability was observed in most films even when the particle size was not as large as predicted using the procedure above. For example, film 37Q was stable even when thermally exposed for 67 h at 460°C. SEM photomicrographs, however, showed that the agglomerate size itself was ~ 1000 Å, the Cr particle size must, therefore, be smaller. This suggests that the passivation of Cr in the film is not totally due to the thick layer formed around them but also due to other factors. Pettit et al.[82] suggest that thermally stable films had the Cr particles clustered together to reduce the surface to volume ratio (and, therefore, reduce oxidation). They also reported that the areal density of stable coatings was higher than that of unstable coatings, i.e., stable coatings had a small void volume. The agglomerate size in the black chrome films indicates that clustered Cr particles alone could not have been responsible for thermal stability. Zajac, Ignatiev and their co-workers[31,41] proposed that the thermal degradation was due to the formation of microvoid metallic Cr particles by the evolution of H_2O at temperatures ≤ 300°C. The evolution of H_2O was caused by the decomposition of chromium hydroxides to chromium oxide. Subsequent thermal exposure caused rapid oxidation of these Cr particles. They also proposed that layers of spheroidal Cr particles, each covered with a thin Cr_2O_3 coating, were covered at the surface by a layer of ≈ 400 Å thick loosely packed Cr_2O_3. Thermal exposure caused this layer to grow along with increased oxidation of the particles throughout the film.

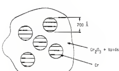

a) As-deposited

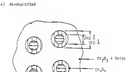

b) 10,000 h at 350°C

Figure 7 3 Effect of thermal exposure on black chrome film with 700 Å Cr particles

The AES depth profiles of black chrome films suggest that the Cr_2O_3 formed close to the surface aids in the passivation of Cr particles deeper in the film. This is similar to that suggested by Ignatiev et al.[31] However, on the basis of their model, oxide content increase would be uniform throughout the inner layers of the film. Such a prediction is not supported by Auger sputter profile data for the films studied here. The Auger data show that increasing oxide content (with thermal exposure) is associated with a thickening of the outer pure Cr_2O_3 layer. This is demonstrated in Figures 5.4 - 5.6. Both figures show the advancement of the oxide layer into the film with increasing thermal exposure. It should be noted that some increase in oxide content is observed within the film, but that increase is less with increasing depth into the film. There are at least two different modes of change in microstructrue that can be proposed that exhibit this behavior.

The first type of microstructure is such that the as-deposited oxide is more passivating deep inside the film than it is closer to the surface. In other words, the interconnected void distribution is non-uniform, being large close to the surface and progressively decreasing with depth. Note that this does not imply that the total void volume (interconnected plus isolated) decreases with depth, no data are available on this question. In the second type of microstructure, the film is viewed as having voids distributed throughout the film. Initial stages of thermal exposure cause rapid oxidation. Most of the oxide forms by oxidation of Cr particles closest to the surface, although some oxide will be formed on Cr particles deeper inside the film (due to the parous nature of the films). Thickening of the outer layer of oxide (with increasing thermal exposure) protects the

Cr particles deeper inside the film. The growth of the oxide causes the closure of pores wherever the oxide forms. The void volume distribution thus becomes non-uniform.

Although neither type of suggested microstructural changes can be considered to be implausible, experimental evidence favors the former, i.e., the structure with void distribution shown in Figure 7.4. The distribution of Cl contamination (discussed in the next section) suggests an interconnected void distribution, such as shown in Figure 7.4.

Auger sputter data clearly support the contention that the nickel substrate is not oxidized until all of the black chrome film is oxidized. Irrespective of the black chrome film being analyzed, the oxygen Auger peak (associated with oxide formation) never showed an increase at the interface (indicating formation of NiO) before near complete oxidation of the film. This indicates that the black chrome film is passivating towards NiO formation. The fact that Cr_2O_3 increased deep within the coating but NiO was not observed implies that although there are voids between the agglomerate, few interconnected voids extend completely to the interface. Some such voids must exist from the interface to the center of the black chrome films or deeper, resulting in the increased Cr_2O_3 content at depths greater than half the film thickness.

Effect of Minor Constituents in the Film

Several of the black chrome films had Cl present (Chapter V). This Cl desorbed easily during thermal exposure, evident from data presented in Chapter V. Thermal desorption studies showed that the Cl began to desorb (primarily as HCl^+) at temperatures as low as 200°C. The rate of desorption

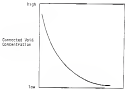

Figure 7.4 Schematic distribution of connected void distribution as a function of depth into the film

increased with increasing temperature up to ~ 500°C (Figure 5.9). Although thermal desorption of H_2O and H species was also observed, it was not clearly attributable to the sample. Smith et al.[40] observed desorbed H_2O and H species and attributed them mainly to the presence of chromium compounds rather than to chemisorbed species. They analyzed as-prepared electrodeposited black chrome films and after thermal exposure for 1 h in air. The samples were re-examined after atmospheric exposure for any re-adsorption of water. Little or no water was observed to re-adsorb. They argued that the irreversible nature of the removal of H_2O and H meant that the thermally desorbed H_2O and H species were from hydrogen containing compounds of chromium. However, it is not clear from their procedure and results if they considered the possibility of H_2O and H being adsorbed during sample preparation. As the procedure in Appendix B indicates, there are several stages after electrodeposition that involve cleaning with water. Such steps could encourage H_2O chemisorption, or condensation in capillaries, particularly in films that contain interconnected voids. Thermal exposure would cause rapid desorption and, unless these films were again immersed in water, the extent of re-adsorption (in air) would be much smaller. This is important since, as discussed earlier in this chapter, they model the thermal degradation mechanism as being related to the formation of microvoids during thermal evolution of H_2O and H.

Chlorine in the films studied could have been incorporated during electrodeposition or in the subsequent cleaning operations. The Auger sputter profiles of all the Cl containing films showed large Cl Auger signals at the surface, but this signal intensity decreased rapidly with increasing depth into the film. The incorporation of Cl during electrodeposition can be explained by suggesting that Cl forms a positive ion complex with Cr and is deposited into the film. But Pettit and Sowell[32] reported that even high levels of Cl contamination in the electrodeposition bath did not cause Cl to be present in the films. They observed that high Cl contamination in the bath detrimentally affected the thermal stability of black chrome films because the films formed large isolated clusters of Cr and Cr_2O_3 rather than a uniform film. SEM photomicrographs of black chrome films, with Cl contamination, such as 37Q, showed that such films had the same densely packed structure as the non-Cl containing films. In fact, film 37Q, which had Cl, was one of the most stable films.

Thus, it appears that a second effect of Cl, different from that reported by Pettit and Sowell, was observed in this study. It seems likely that the Cl detected in the films in this study was adsorbed during the wash cycles after electrodeposition (Appendix B). Concentrations of Cl in the cleaning baths were likely due to build-up from the solution brought in by the black chrome film and holder after every deposition. Adsorption in the washing baths would explain the decreasing concentration of Cl with increasing depth into the film. The presence of voids would permit migration of Cl into the film but migration becomes less likely as the depth into the films becomes larger. Furthermore, Cl was not concentrated at the film-substrate interface, supporting the earlier conclusion that few interconnecting paths exist all the way to the interface. Note that both the proposed microstructural change modes (see preceding section) can explain the decreasing concentration of Cl with depth into the film and the relative ease with which Cl desorbed on thermal exposure.

Comparison with Model Calculations

A comparison of the experimental results and the model calculations discussed in Chapter II show that there is good qualitative agerement with the model of Sweet and Pettit.[32] The experimental reflectance curves, plotted in Figures 4.6 - 4.19, all show the broad adsorption edge at wavelengths > 1 μm and a relatively flat reflectance profile at lower wavelengths. However, on thermal exposure, most of these films exhibit a broad reflectance maxima at ~ 0.8 μm (in addition to the absorption edge). The maxima both increased and shifted to lower wavelengths (e.g., Figure 4.7). Based upon theoretical calcualtions (Chapter II), this broad maxima is associated with the formation of a passive layer around the metallic Cr particles. The reduction in the Cr particle size (due to oxidation) and the formation of the dense passive Cr_2O_3 layer around it result in changes in the extent of interaction of the film with incident radiation, thereby changing the reflectance curves.

From Sweet and Pettit's reflectance calculations (Figure 2.11), the increase in the broad maxima at ~ 1 μm is approximately related to the increase in oxide content in the film. On the basis of the relative peak heights at 1 μm, the relative volume fractions of Cr to (Cr + Cr_2O_3) should be 0.2, 0.31, 0.45 and 0.58 instead of 0.2, 0.3, 0.4 and 0.5, the volume fractions used to calculata the reflectance curves in Figure 2.11. However, the experimental reflectance curves plotted in Figures 4.6 - 4.19 show no such correlation between the relative volume fraction of Cr to (Cr + Cr_2O_3) and the relative peak heights of the broad maxima. This suggests that the idealized model of coated spherical particles embedded in an insulating medium only qualitatively agrees with the real structure. Model calculations assumed that the void distribution (and volume) and agglomerate size all remained constant irrespective of the deposition conditions and with thermal exposure. Experimental data do not support these assumptions. Experimental evidence in association with model calculations suggest the following:

a) The deposition conditions control the void volume, agglomerate size and possibly the void distribution. Films with lower as-deposited oxide contents are generally associated with lower void volumes.[22]

b) Thermal exposure causes non-uniform oxidation of the film. The Cr_2O_3 surface layer thickens with increasing oxidation. Deeper layers only show smaller changes in oxide content.

c) The non-uniform oxidation behavior is due to the non-uniform distribution of voids or changes in the distribution of voids in the film.

Thus, model calculations assuming uniformity of void distribution, etc., can give only qualitative correlations with real films. More quantitative results should be obtained by considering model film structures that exhibit non-uniform void volumes, dense Cr_2O_3 outer layer and a distribution of coated spherical Cr particles within the film. Such model calculations are not affected by whether the non-uniform void volume is a result of thermal exposure or intrinsic to the film. There are, however, many difficulties in incorporating the effects of void volume and distribution changes into model calculations, as explained in Chapter II. However, such incorporation is necessary to better predict the behavior of real black chrome films.

Effect of Deposition Conditions

The optical properties and the thermal stability of the black chrome films are directly controlled by the electrodeposition conditions, such as those listed in Table 3.1. Variation in the deposition parameters affects the visual appearance of these films as well as their behavior during thermal exposure

Appearance of Black Chrome Films

The black chrome films, deposited under conditions listed in Table 3.1, show noticeable differences in appearance Coatings 21A through 22B are grayish-white in color while films 29D, 29E and 29J have a streaked look. The other films have a uniform appearance, their color ranging from dark blue to a dull black

The grayish-white films (21A - 22B) also were very thin (≤ 200 Å) and had very low oxide content. Their deposition was associated with less vigorous evolution of gas at the cathode A comparison of the deposition conditions (Table 3.1) does not show any significantly different parameters The CrO_3 concentration of the bath used for these films is the lowest (171 ~ 179 g/l) but only slightly lower than the baths used to deposit dark films (≥ 181 g/l). It was suspected that a likely reason for the metallic nature of these black chrome films was due to sulfate contamination. However, sulfate concentration was not measured. Deliberate addition of - 0.5 g/l of sulfate ions into a black chrome bath immediately caused the formation of grayish deposits, which confirmed initial suspicions. Similar baths containing sulfate concentrations ≥ 2 g/l are used for depositing Cr metal coatings.[127] In addition to ≥ 2 g/l of sulfate ions, metal Cr electrodeposition baths contain ≥ 250 g/l of CrO_3 and are deposited at current densities > 350 mA/cm^2 from baths maintained at temperatures ≥ 50°C. Comparison with the deposition conditions for the grayish-white coatings (21A- 22B) explains the thinness of these coatings. They are deposited at lower current densities and from lower temperature baths, both of which reduce the deposition rate. Furthermore, high CrO_3 to sulfate ion concentrations result in low deposition rates. It is expected that the sulfate concentration in these black chrome baths, though significant, would be much less than in the metallic Cr deposition baths (≥ 2 g/l). Therefore, the CrO_3 for sulfate ion ratio is likely to be higher, resulting in poorer deposition rates.

The presence of sulfate ions in the baths can be attributed to a gradual build-up of its concentration with use. Furthermore, there was a gap of several days between the previous batch of depositions and the 21A - 22B group. Besides build-up of sulfate contamination, this period of time may have enabled any undissolved sulfates to dissolve as well. The next batch of black chrome films was also deposited from this bath. However, the bath was diluted to more than twice its volume and fresh additions of barium carbonate (to precipitate out sulfates from the bath), CrO_3 and acetic acid were made. Subsequently, these black chrome films showed the dark color (associated with higher oxide content) and were much thicker than the grayish-white coatings.

The most important feature associated with the electrodeposition of the "streaked" films (29D, 29E and 29J) was higher temperature. They were deposited at 28 - 30°C, while all the other films were deposited from baths at temperatures < 25°C. The higher bath temperature appears to have caused more intense foaming at the cathode, resulting in non-uniform thickness films.

Chromic and Acetic Acid Concentration

Chromic acid is the principal source for the chromium deposited in the black chrome films, while the primary role of acetic acid is that of a buffer (i.e., to maintain the pH). Although varying either CrO_3 or acetic acid affects the nature of the deposit, the combined action is equally important. For example, chromic acid concentrations (≥ 400 g/l) have been reported to produce grayish deposits.[34,36] However, black chrome films (29D, 29E and 29F) deposited from high CrO_3 concentration baths were bluish-black in color. The reason for this is that these had acid concentrations < 20 vol %, unlike the baths reported to produce grayish deposit which had ~ 27 vol %. The low acetic acid concentration compensated for the high CrO_3 acid concentrated and produced a dark deposit. The combined interaction of acetic and chromic acid on the volume fraction of oxide in the deposition conditions shown in Table 3.1. These data are based on the deposition conditions' oxide contents, shown in Table 3.1. The values in Table 7.1 show that a combination of high CrO_3 or low CrO_3 with optimum acetic acid concentration (25 - 28%) resulted in as-deposited oxide content of 40 - 50%. Optimum CrO_3 concentration (300 - 350 g/l) caused the as-deposited oxide content to decrease to 30 - 40%.

Fe^{+3} Concentration

The presence of Fe^{+3} in the electrodeposition bath was due to deliberate additions of iron oxalate to reduce Cr^{+6} to Cr^{+3} and/or dissolution

Table 7.1 Variation of As-Deposited Film Oxide Content with Acetic Acid and CrO_3 Acid Concentrations in the Electrodeposition Bath

Acetic Acid (vol.%)	CrO_3 (g/l)	As-Deposited Cr_2O_3
15	350	40~45
15-20	200-300	40-45
20-25	200	45~50
	350	40~50
25-28	200	45~50
	200-300	45~50
	300-350	30~40

of the mild steel anode. Pettit et al.[82,92] observed no significant effect of Fe^{+3} concentrations of < 8.5 g/l on the black chrome films except for a small increase in the solar absorptance (≤ 1%) with decreasing Fe^{+3} concentrations. However, higher concentrations were observed to cause codeposition of Fe. The Fe^{+3} concentrations used in this study were ≤ 7.6 g/l. No Fe was deposited in any of these black chrome films. Variation in optical properties (or oxide content) were evidently more related to changes in the other deposition parameters than to changes in Fe^{+3} concentrations.

Cr^{+3} Concentration

The concentration of Cr^{+3} in the bath is directly related to the Cr_2O_3 content of the as-deposited black chrome film. Figure 7.6 is a plot of the variation of the as-deposited Cr_2O_3 content of the different films as a function of Cr^{+3} concentration in the bath. Note that at low Cr^{+3} concentrations (≤ 7 g/l), the oxide content in the as-deposited film is ≥ 40%. The oxide content decreases to 30 ~ 40% when the Cr^{+3} concentration is 7.0 ~ 8.5 g/l. At 16 g/l concentration, the Cr_2O_3 content was observed to be 40 ~ 50%. This is true even when comparing films deposited from baths where the other parameters (CrO_3, acetic acid, etc.) were not held constant. The effect of Cr^{+3} concentration in the bath on the oxide content is not completely independent of the other variables. Pettit et al.[82] reported that low Cr^{+3} concentrations (≤ 6.5 g/l) in a bath with acetic acid concentration of ~ 27 vol.% and CrO_3 concentration of ~ 330 g/l produced gray coatings. Reduction in the CrO_3 concentration, however, resulted in bluish coatings, as was observed in this study.

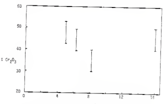

Figure 7.5 Variation of as-deposited Cr_2O_3 with Cr^{+3} concentration in the electrodeposition bath

Current Density and Deposition Time

These two parameters principally affect the deposition rate and the film thickness. Increasing the deposition time increased the film thickness. The effect of increased film thickness was to shift the absorption edge to longer wavelengths (see preceding sections)[12]. This resulted in increased solar absorptance although the thermal emittance also increased. For example, 37Q, which was thicker than 37F had its absorptance edge at ~ 1.6 μm rather than ~ 1.4 μm (for 37F), higher solar absorptance (as can be deduced from the reflectance curves) and higher thermal emittance (0.173 for 37Q and 0.098 for 37F).

The current density affects the film thickness by affecting the deposition rate. For example, films 29Ba and 29C were deposited under identical conditions, except that 29C was deposited at 193 mA/cm^2 and 29Ba at 176 mA/cm^2. Although both had the same volume fraction of oxide, comparison of the reflectance data showed that 29Ba degraded more rapidly than 29C. Auger sputter data showed that film 29C was ~ 25% thicker than 29Ba and this increased thickness was responsible for the improved thermal stability.

Optimum Deposition Conditions

The optimum deposition conditions, on the basis of their effect on the optical properties and thermal stability are those with which film 37Q were deposited. They are as follows:

CrO_3	306.2 g/l
Acetic Acid	26.84 vol %
Cr^{+3}	8.5 g/l
Fe^{+3}	6.92 g/l

Temperature	20 - 25°C
Current density	184 mA/cm^2 for 5 minutes

Pettit and Sowell[92] have suggested optimum deposition conditions as follows

CrO_3	332 ± 4 g/l
Acetic Acid	27 ± 1 vol %
Cr^{+3}	8 ± 0.5 g/l
Fe^{+3}	7.5 ± 1 g/l
Current Density	188 mA/cm^2 for 3 - 5 minutes
Temperature	18 - 26°C

Comparison of the deposition conditions for 37Q with those suggested by Pettit and Sowell show that they match well, except that 37Q was deposited with slightly lower CrO_3 concentration. This indicates that the concentration ranges suggested by Pettit and Sowell may be more restrictive than necessary. However, their suggested range of deposition parameters (with the exception of CrO_3) did produce the most stable black chrome films

CHAPTER VIII
CONCLUSIONS

The results discussed in the previous chapters show that the properties of the black chrome film are dependent on the deposition conditions. Optimum deposition conditions, derived on the basis of the optical properties and thermal stability, are similar to those recommended by Pettit and Sowell,[92] except that chromic acid concentration is less (306 g/l instead of 332 g/l).

In this study, the compositions of the black chrome films were calculated from Auger sputter depth profiles and XPS data. Sputter reduction of Cr_2O_3 to Cr was observed, but remained constant after ~ 1 minute of sputtering (< 50 Å). Sputter reduction of Cr_2O_3 was accounted for in data reduction. Differential sputtering of Cr_2O_3 relative to Cr was also observed, but the effect on sputter profiles was shown to be negligible. The oxide contents calculated from AES and XPS data showed good precision (± 5%), indicating that the method used for quantification was reasonable.

Black chrome films followed logarithmic oxidation behavior when thermally exposed, i.e., rapid oxidation during the first few hours of thermal exposure followed by increasingly slower oxidation. This was observed even though the as-deposited films contained 30 - 50% oxide. Therefore, the as-deposited oxide was generally non-passivating and only oxide formed during thermal exposure would protect the Cr particles from further oxidation. The oxidation behavior of black chrome is similar to that of pure bulk Cr. Oxidation data obtained on pure Cr can hence be used to predict the stability of black chrome films.

The solar absorptance of black chrome films was directly related to the oxide content. It remained constant at its maximum value when the oxide content was in the range of 40 ~ 75% (± 5%) during service. Below and above this range, solar absorptance decreased rapidly. Therefore, as-deposited films that had ~ 30% oxide were the most stable since thermal exposure raised their oxide content into the optimum range. Films with 40 ~ 50% as-deposited oxide degraded rapidly during thermal exposure since their oxide content increased rapidly to > 80%.

While the solar absorptance was principally controlled by the composition and structure of these films, the thermal emittance was more dependent on the optical properties of the substrate. The high reflectance of metal substrates at long wavelengths (2 ~ 20 μm) is the main reason for the low emittance of these absorbers. However, increasing film thickness and decreasing oxide content (within the optimum range) increases the thermal emittance due to a shift in the absorption edge to longer wavelengths and due to larger amounts of multiple scattering between particular Cr.

Model calculations suggest that the Maxwell-Garnett theory can be extended to predict the behavior of black chrome films. The microstructural model comprised of a sphere of Cr metal coated with dense Cr_2O_3 embedded in a matrix of voids and amorphous Cr_2O_3 gave dielectric constants that predict reflectance (and absorptance) values similar to those experimentally observed. However, non-incorporation of effects such as void volume/distribution and agglomerate size/distribution limits the accuracy of the predictions. Furthermore, experimental evidence suggests that these films are not as simple as those used for model calculations. The real films have a dense outer Cr_2O_3 layer covering a structure of agglomerates. Thermal exposure causes a non-uniform increase in oxide content in the film. The thickness of the outer Cr_2O_3 layer increases with increasing oxide content, although there is a somewhat smaller increase in oxide content within the film as well. Such non-uniform increases must be incorporated for any model calculations to be realistic. The void volume and distribution is either non-uniform in the as-deposited films or becomes so with thermal exposure, indicating an inherent limitation in all model calculations to date.

The primary area in which additional experimental data is required is with respect to voids. Knowledge of their volume and distribution is essential before any improvements can be envisaged. By changing the void content/distribution, the optical properties and the thermal stability can both be altered. Experimental data presented in this study suggest that such species as Cl can be used to determine (connected) void distributions while areal density measurements can be used to obtain total void volume.

Theoretical model calculations are presently limited by their assumptions of uniform void volume/distribution and oxide content variation in the film. As shown in this study, void volume/distribution is clearly non-uniform. Its effect must, therefore, be incorporated. Better modeling of the oxide content distribution in black chrome films is necessary before model calculations can be considered realistic. The distribution of oxide is, again, clearly different from that assumed in model calculations to date.

APPENDIX A
BRUGGEMAN SYMMETRICAL EFFECTIVE MEDIUM (BEM) THEORY

This is the second major theory of dielectric functions for a complex media.[48,49] In this theory, the matrix and the particles are treated on an equal basis, i.e., they are both considered to be in particulate form and approximately symmetrical to each other.

The BEM dielectric constant can be derived from the model shown in Figure A.1.[32,43] Consider that the particles are spherical and that they are embedded in a uniform medium with an effective dielectric constant, ϵ_B. For a field $\bar{E}_0$ far from the particle, the dipole moment associated with the volume under consideration is[43]

$$\bar{p} = \frac{3}{4\pi} V \left[\frac{\epsilon_1 - \epsilon_2}{\epsilon_1 + 2\epsilon_B}\right] \bar{E}_0 \tag{A-1}$$

where

V = volume of the region, and

ϵ_1 = dielectric constant of the particle.

This polarization produces a deviation from $\bar{E}_0$, whose space integral is $-4\pi\bar{p}$.[43,68] For two types of particles (see Figure A.1), the net polarization must be zero, i.e.,

$$f_1 \frac{\epsilon_1 - \epsilon_B}{\epsilon_1 + 2\epsilon_B} + f_2 \frac{\epsilon_2 - \epsilon_B}{\epsilon_2 + 2\epsilon_B} = 0 \tag{A-2}$$

where

f_1, f_2 = volume fractions of particles 1 and 2 in Figure A.1, respectively (particle and matrix in our case) [$f_1 = 1 - f_2$]

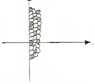

Figure A 1 Bruggeman Composite. The particles (shaded regions) and the matrix (clear regions) are assumed to be topologically equivalent and randomly distributed

$\varepsilon_1, \varepsilon_2$ = dielectric constants for particles 1 and 2, respectively

Solving equation (A-2),

$$\varepsilon_B = \frac{1}{4}\,[\gamma + (\gamma^2 + 8\varepsilon_1\varepsilon_2)^{1/2}] \qquad \text{(A-3)}$$

where

$$\gamma = (3f_2-1)\varepsilon_2 + (3f_1-1)\varepsilon_1$$

This equation can be generalized for any number of components, viz ,

$$\sum_i f_i \left[\frac{\varepsilon_i-\varepsilon_B}{\varepsilon_i+2\varepsilon_B}\right] = 0 \qquad \text{(A-4)}$$

The above equation is valid only for spherically shaped components. The approach can be generalized for ellipsoids,[32,129] resulting in

$$\sum_i \frac{f_i}{L_i\frac{\varepsilon_i}{\varepsilon_B} + (1-L_i)} = 1 \qquad \text{(A-5)}$$

where L_i is the depolarizing factor for the ith type particle. Since equation (A-5) is not a linear equation in ε_B, solutions based on it have been restricted to cases that can be solved.

The results obtained with the BEM theory and the MG theory are quite different.[72] Although the two theories can lead to the same result (under certain conditions),[72,130] MG's approach is considered more suitable for cases where the film structure is well described by a matrix having a distribution of spherical inclusions. In other words, MG theory is more appropriate for situations topologically equivalent to the case where the dielectric is constrained to have a distribution of spherical inclusions.[72] On the other hand, the BEM theory should be considered more suitable for systems where the constituent materials enter on an equal basis.[72]

APPENDIX B
PROCEDURE FOR DEPOSITION OF BLACK CHROME FILMS ONTO NICKEL PLATED PLAIN CARBON STEEL SUBSTRATE

1) Cut substrate to desired size (~ 85 x 80 mm).
2) Vapor degrease in trichloroethylene for more than 15 minutes.
3) Etch in fresh aqua regia for 5 minutes. Mount in substrate holder (Figure 3.3).
4) Soak in agitated Alconox solution for about 15 minutes.
5) Immerse in agitated 71 g/l NaOH solution at 65 - 80°C for 1 - 2 minutes.
6) Rinse in tap water (by immersion) for 2 - 3 minutes.
7) Immerse in 10% H_2SO_4 solution at room temperature for 1 - 3 minutes.
8) Rinse in tap water (by immersion) for 2 - 3 minutes.
9) Rinse in deionized and distilled water (by immersion).
10) Spray rinse with deionized and distilled water.
11) Rinse in deionized and distilled water (by immersion).
12) Electrodeposit black chrome using the apparatus shown in Figure 3.2.
13) Rinse in deionized and distilled water (by immersion).
14) Spray rinse with deionized and distilled water.
15) Rinse in deionized and distilled water (by immersion).
16) Blow dry.

The various solutions and distilled water baths must be changed frequently to avoid contamination and loss in effectiveness. One important precaution that must be followed is that the substrate must not be allowed to dry between the procedural steps. Also, no more than the specified time must be allowed for each step, otherwise poor adhesion of the deposit results.

APPENDIX C
ANALYSIS OF THE ELECTRODEPOSITION BATH

The procedure, outlined below for determining the Cr^{+3} concentration, Fe^{+3} concentration, chromic acid content and acetic acid content are based on those suggested by Erickson.[131] Briefly, the Cr^{+3} concentration is determined by measuring the transmittance at 590 nm and correlating that to Cr^{+3} concentration on a standard curve. The Fe^{+3}, CrO_3 and acetic acid concentrations are obtained from titrations against standard solutions.

Cr^{+3} Concentration

a) Filter plating bath solution
b) Transfer 5 ml to a 100 ml volumetric flask
c) Add 0.4 ml concentrated phosphoric acid (85%)
d) Make up to 100 ml with distilled water and mix
e) Transfer to curette
f) Set spectrophotometer wavelength at 590 nm and distilled water transmittance at 100%
g) Measure the transmittance of the unknown samples.
h) Read off the Cr^{+3} concentration in g/l from a standard curve (shown in Figure C.1)

The standard curve was obtained as follows

a) 5.658 g of pure $K_2Cr_2O_7$ was dissolved in 400 ml distilled water (in a 600 ml beaker).
b) 2 ml concentrated H_2SO_4 acid was added and mixed well

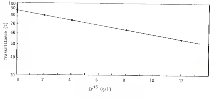

Figure C.1 Standard curve for change in transmittance as a function of Cr^{+3} concentration.

c) Sulfur dioxide gas was bubbled through the solution for more than half an hour. This reduced all the Cr^{+6} to Cr^{+3}.
d) The solution was then heated to near boiling for more than 2 hours to remove all excess SO_2.
e) The cooled solution was then diluted to 1 liter in a volumetric flask. This solution contained 2 mg Cr^{+3} per ml.
f) Standard solutions were then made using this solution in 100 ml volumetric flasks, as shown in Table C.1. The table also shows the other constituents added.

The additions of $K_2Cr_2O_7$, acetic acid and phosphoric acid were used to simulate the presence of Cr^{+6} and the acids in the electrodeposition bath. Phosphoric acid reduces the interference due to Fe^{+3} (in the bath) at the transmitted wavelength. The instrument used for measurement of transmittance was a Perkin-Elmer UV-VIS spectrophotometer (double beam) with wavelength set at 580 nm (1 nm slit).

Analysis of CrO_3, Acetic Acid and Fe^{+3} Concentration

The procedures followed for analysis of these three constituents are shown in block diagram form (Figure C.2). The equations used to calculate the concentrations are as follow:

$$CrO_3 \text{ (g/l)} = M \times N \times 83.317 \qquad \text{(C-1)}$$

$$\text{Acetic Acid (vol.\%)} = \frac{100}{A}\left(B \times D - \frac{C}{50}\right) \qquad \text{(C-2)}$$

$$Fe^{+3} \text{ (g/l)} = T \times E \times 55.847 \qquad \text{(C-3)}$$

Table C.1 Composition of Solutions Used to Obtain Standard Curve (Figure C.1)

Additions to Make Up Standard Solution				
Cr^{+3} ml of 2 mg/ml soln.	H_3PO_4	Acetic Acid	$K_2Cr_2O_7$	Equivalent Cr^{+3} in bath
0	0.4 ml	1.1 ml	2.5 g	0
5 ml	0.4 ml	1.1 ml	2.5 g	2 g/l
10 ml	0.4 ml	1.1 ml	2.5 g	4 g/l
20 ml	0.4 ml	1.1 ml	2.5 g	8 g/l
30 ml	0.4 ml	1.1 ml	2.5 g	12 g/l

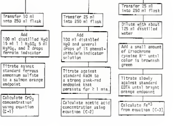
Dilute 40 ml plating solution to 1 liter in volumetric flask
Transfer 10 ml into 250 ml flask
Add 100 ml distilled H_2O 15 ml 1 1 H_2SO_4 5 ml H_3PO_4, and 2 drops ferroin indicator
Titrate against standard ferrous ammonium sulfate to a salmon orange endpoint
Calculate CrO_3 concentration using equation (C-1)
Transfer 25 ml into 250 ml flask
Add 100 ml distilled H_2O and several drops of 1% phenolphthalein indicator solution
Titrate against standard NaOH to a strong pink-red endpoint that persists for ≥ 1 min
Calculate acetic acid concentration using equation (C-2)
Transfer 25 ml into 250 ml flask
Dilute with about 125 ml distilled water
Add a small amount of Eriochrome cyanine R" until color is brownish green
Titrate slowly against standard EDTA until bright orange endpoint
Calculate Fe^{+3} from equation (C-3)

Figure C.2 Procedure for analysis of CrO_3, acetic acid and Fe^{+3} in black chrome electrodeposition baths

where

M = ml of standard ferrous ammonium sulfate,

N = normality of standard ferrous ammonium sulfate (0.1 N),

A = molarity of acetic acid used (17.5),

B = ml of standard NaOH,

D = normality of standard NaOH (0.5 N),

C = CrO_3 concentration (g/l) determined for the bath using equation (c-1),

T_2 = ml of ethylenediamine tetraacetate (EDTA) solution, and

E = molarity of EDTA solution (0.1 M).

The standardization of the solutions (titrants) was done using procedures listed in almost all standard chemistry texts.[132]

APPENDIX D
QUANTIFICATION OF AUGER SPUTTER DATA

The formula used in Chapter V (equation (5.1)) to calculate the volume fraction of Cr_2O_3 in the black chrome films is derived on the basis of the following assumptions.

1) The Auger Cr signal detected (at any instant) from the black chrome film is a summation of the signals due to the metallic Cr and Cr as Cr_2O_3 in that segment of the film being analyzed.
2) The Cr peak height of the detected signal varies linearly with the amount of oxide.
3) Sputtering rate is constant for mixtures of Cr and Cr_2O_3.
4) All the oxide present in the film is Cr_2O_3. There is no Ni oxide formed until the black chrome film is completely oxidized.

The assumptions are reasonable, with one exception. The different constituents are assumed to sputter at the same rate, i.e., differential sputtering is not considered. Experimental evidence suggests that Cr_2O_3 sputters twice as fast as Cr. Therefore, any equation derived on the basis of these assumptions gives results which, though reasonable, are not completely quantitative.

The volume fraction oxide in the film segment being analyzed is

$$f_{Cr_2O_3} = \frac{(I_{Cr})_{Cr_2O_3}}{I_C} \qquad (D\text{-}1)$$

where

$(I_{Cr})_{Cr_2O_3}$ is the peak intensity of Cr due to Cr_2O_3, and I_C is the total Cr peak intensity detected.

Since the peak height is assumed to vary linearly with the amount of oxide, the oxygen peak height can be used for determining the oxide content

Let

$$M = \frac{(I_{Cr})_{oxide}}{(I_{Cr})_{metal}}$$

and

$$R = \frac{(I_{Cr})_{oxide}}{(I_{O})_{oxide}}$$

where $(I_{Cr})_{metal}$ refers to the Cr signal peak height in pure Cr, $(I_{Cr})_{oxide}$ to the Cr signal peak height in pure Cr_2O_3 and $(I_O)_{oxide}$ to the O signal peak height in pure Cr_2O_3. The values of M and R, determined experimentally on the AES system used are

$$M = 0.37$$

$$R = 0.46$$

Substituting in equation (D-1)

$$f_{Cr_2O_3} = \frac{(I_{Cr})_{Cr_2O_3}}{(I_{Cr})_{Cr_2O_3} + (I_{Cr})_{Cr}} \qquad (D-2)$$

or

$$f_{Cr_2O_3} = \frac{I_O R}{I_O R + (I_C - I_O R)M} \qquad (D-3)$$

where $(I_{Cr})_{Cr}$ is the Cr peak intensity due to metallic Cr

Since it is being assumed that the sputtering rate is constant for a mixture of Cr and Cr_2O_3 and that no nickel oxidation is occurring, the area under the oxygen and chromium sputter profiles from the black chrome sample can be substituted for intensities. This will permit determination of the volume fraction of Cr_2O_3 in the entire film, i.e.,

$$f_{Cr_2O_3} = \frac{A_O R}{(A_{Cr} - A_O R)M + A_O R} \qquad (D\text{-}4)$$

where A_O and A_{Cr} represent the areas under the O and Cr AES sputter profiles, respectively. Equation (D-4) is the equation used in Chapter V (equation (5.1)) to calculate the oxide contents. It should be noted that the experimental value of 0.37 for M is consistent with the assumptions used to derive equation (D-4). This is because M would equal 0.4 when Cr is converted to Cr_2O_3.

APPENDIX E
EFFECT OF SiO_2 OVERLAYER ON BLACK CHROME OXIDATION

Electrodeposited black chrome coatings exhibited constant and high values of α_s when the Cr_2O_3 was maintained between 40 – 75%. To determine the effect of an overlayer on the oxidation of black chrome films when thermally exposed, some of the films were coated with a thin layer of SiO_2. The overlayer was thermally evaporated onto the black chrome films in a vacuum system where the residual pressure was $\leq 2 \times 10^{-6}$ Torr. The overlayer of SiO_x became SiO_2 after a short period of thermal exposure. SiO_2 was identified from the characteristic AES chemical shift of Si.[133]

Typical AES sputter profiles of a SiO_2-coated black chrome film is shown in Figure E.1. Si is seen to be restricted close to the surface although increased thermal exposure caused gradual diffusion of Si into the bulk of the black chrome film. Assuming that all the Si is present as SiO_2, the amount of Cr_2O_3 was calculated using equation (5.1), but after compensating for the presence of SiO_2. The integrated oxygen area was modified using

$$A'_O = A_O - A_{Si}R \tag{E-1}$$

here A'_O is the modified integrated area, A_O is the total oxygen integrated area, A_{Si} is the area under the Si profile and R is the ratio of the O to Si Auger peak heights in SiO_2 (R = 0.46). A'_O was the value used in equation (5.1) instead of A_O.

The effect of the SiO_2 overlayer on the oxidation of black chrome is evident from the plots shown in Figure E.2. The oxide content as a function of thermal exposure of two black chrome films, with and without SiO_2 is

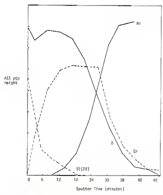

Figure E 7 AES sputter profile of black chrome film SBN-11 coated with SiO_2 and thermally exposed for 1 h at 395°C

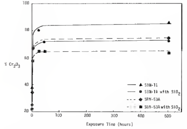

Figure E 2 Effect of SiO_2 overlayer on the Cr_2O_3 content in black chrome films as a function of thermal exposure at 395°C.

plotted. Both the films show that although the behavior was still logarithmic, the SiO_2 overlayer reduced the amount of Cr_2O_3 in the film at any specific time-temperature combination. Pettit and Brinker[125] subsequently observed a similar effect when a sol-gel coating was used.

The results indicate that an overlayer of SiO_2 reduces the Cr_2O_3 content of the black chrome film upon thermal exposure, but does not change the rate limiting mechanism for oxidation.

REFERENCES

1. B. O. Seraphin, 'Spectrally Selective Surfaces and Their Impact on Photothermal Solar Energy Conversion,' in Topics in Applied Physics, Vol. 31, Solar Energy Conversion, B. O. Seraphin, ed., Springer-Verlag (1979).

2. P. J. Call, "Overview of Solar Energy Conversion Technologies Quantum Processes and Thermal Processes,' in Basic Research Needs and Opportunities on Interfaces in Solar Materials, A. W. Czanderna and R. J. Gottschall, eds., Proc. July 1980 Workshop, U. S. Department of Energy.

3. D. M. Mattox, 'Optical Materials for Solar Energy Applications,' Optic News (Summer, 1976).

4. M. L. Day, O. S. Remer and D. Hyatt, SAMPE Quarterly (Oct. 1979), 28.

5. K. Graff and H. Fischer, "Carrier Lifetime in Silicon and its Impact on Solar Cell Characteristics," in Topics in Applied Physics, Vol. 31, Solar Energy Conversion, B. O. Seraphin, ed., Springer Verlag (1979).

6. C. E. Backus, J. Vac. Sci. Technol., 12 (5) (1975), 1032.

7. J. H. Apfel, J. Vac. Sci. Technol., 12 (5) (1975), 1016.

8. R. B. Pettit and R. R. Sowell, J. Vac. Sci. Technol., 13 (2) (1976), 596.

9. B. O. Seraphin, Thin Solid Films, 57 (1979), 293.

10. J. Jurrison, R. E. Peterson and H. Y. B. Mar, J. Vac. Sci. Technol., 12 (5) (1975), 1010.

11. J. C. C. Fan, Thin Solid Films, 54 (1978), 139.

12. O. P. Agnihotri and B. K. Gupta, Solar Selective Surfaces, Wiley-Interscience (1981).

13. R. R. Sowell and R. B. Pettit, Proc. U.S. Dept. of Energy--Division of Solar Technology Thermal Power Systems Workshop on Selective Absorber Coatings, Solar Energy Research Institute, Golden, CO (Dec. 6-8, 1977), p. 175.

14. H. Tabor, Trans. Conf. Use Solar Energy, 2, 1A (1955), 32.

15. H. Tabor, "Research on Optics of Selective Surfaces," Final Report AF61(052)-279, Cambridge Res. Lab. (May, 1959).

16. J. T. Gier and R. V. Dunckle, Trans. Conf. Use Solar Energy, 2, 1A (1955), 41.

17. H. Tabor, Bull. Res. Counc. Isv., A5 (1956), 119.

18. A. J. Sievers, "Spectral Selectivity of Composite Materials," in *Topics in Applied Physics, Vol. 31, Solar Energy Conversion*, B. O. Seraphin, ed., Springer-Verlag (1979)

19. C. M. Lampert and J. Washburn, Proc. 2nd Annl. Conf. on Absorber Surfaces for Solar Receivers, Boulder, CO, Jan. 24, 1979 in Rep. SERI/TP-49-182, 1979, p. 19, Solar Energy Research Institute.

20. O. R. McKenzie, Appl. Phys. Lett., *34* (1) (1979), 25.

21. G. A. Niklasson and C. G. Granqvist, J. Appl. Phys., *50* (8) (1979), 5500.

22. C. G. Granqvist, A. Andersson and O. Hunderi, Appl. Phys. Lett., *35* (3) (1979), 268.

23. L. R. Gilbert, R. Messier and R. Roy, Thin Solid Films, *54* (1978), 149.

24. L. Harris, *The Optical Properties of Metal Blacks and Carbon Blacks*, Monograph series No. 1, The Eppley Foundation for Research, Newport, RI (Dec. 1967)

25. B. Window, I. T. Ritchie and K. Cathro, Appl. Optics, *17* (1978), 2637.

26. R. R. Sowell and R. B. Pettit, "Thermal Aging of Electrodeposited Black Cr," SAND 78-0554, April, 1978, Sandia National Laboratories, Albuquerque, NM

27. J. Hadju and F. Brindisi, Jr., AES Symp. Coatings for Solar Collectors, Atlanta, GA (1976), p. 29.

28. C. V. Bishop and R. Dargis, AES Symp. Coatings for Solar Collectors, Atlanta, GA (1976), p. 109

29. R. B. Pettit, J. Eng. Proc., *100* (1978), 489.

30. R. B. Pettit and R. R. Sowell, Proc. 2nd Annl. Conf. on Absorber Surfaces for Solar Receivers, Boulder, CO, Jan. 24, 1979, in Rep. SERI/TP-49-182, 1979, p. 33, Solar Energy Research Institute, Boulder, CO

31. A. Ignatiev, P. O'Neill and G. Zajac, Solar Energy Mater., *1* (1979), 69.

32. J. N. Sweet and R. B. Pettit, "Optical Modeling of Black Chrome Solar Selective Coatings," SAND 82-0964, 1982, Sandia National Laboratories, Albuquerque, NM

33. G. E. McDonald, Solar Energy, *17* (1975), 119.

34. Harshaw Chromonyx Black Chrome Plating Process, CRX-0270, Harshaw Chemical Company, Cleveland, OH 44106.

35. R. B. Pettit and R. R. Sowell, Proc. 1979 Intl. Solar Energy Society Congr., Atlanta, GA, May 28-June 1, 1979.

36. U. S. Patent 3,620,935 to Harshaw Chemical Company, Cleveland, OH 44106.

37. P. Braun, G. Betz, W. Farber and G. K. Wehner, Proc. 7th Intl. Vac. Congr. and 3rd Intl. Conf. on Solid Surfaces, Vienna, 1977, p. 1825.

38. J. C. C. Fan and S. A. Spura, Appl. Phys. Lett., 30 (1977), 511.

39. G. J. Clark, Z. E. Swithknowski, R. J. Petty and J. C. P. Heggie, J. Appl. Phys., 50 (7) (1979), 4791.

40. G. Zajac, G. B. Smith, A. Ignatiev and J. W. Rabalais, Surf. Sci., 114 (1981), 614.

41. G. Zajac, G. B. Smith and A. Ignatiev, J. Appl. Phys. (submitted).

42. D. M. Mattox, J. Vac. Sci. Technol., 13 (1976), 127.

43. R. Landauer, "Electrical Conductivity in Inhomogeneous Media," in Electrical Transport and Optical Properties of Inhomogeneous Media, J. C. Garland and D. B. Tanner, eds., AIP Conf. Proc. No. 40, Am. Inst. Phys., NY (1978).

44. G. Mie, Ann. Phys. (Leipzig), 25 (1908), 377.

45. M. Kerker, The Scattering of Light and Other Electromagnetic Radiation, Acad. Press, NY (1969).

46. J. C. M. Garnett, Philos. Trans. A, Royal Soc. London, 203 (1904), 385.

47. J. C. M. Garnett, Philos. Trans. A, Royal Soc. London, 205 (1906), 237.

48. D. A. G. Bruggeman, Ann. Phys. (Leipzig), 24 (1935), 636.

49. D. M. Wood and N. W. Ashcroft, Philos. Mag., 35 (1977), 269.

50. I. T. Ritchie, S. K. Sharma, J. Valigraf and J. Spitz, Solar Energy Mater., 2 (1980), 167.

51. G. Zajac, G. B. Smith and A. Ignatiev, J. Appl. Phys., 51 (1980), 6544.

52. R. Chang and W. F. Hall, "On the Correlation Between Optical Properties and Chemical/Metallurgical Constitution of Cr_2O_3/Cr Thin Films," in Electrical Transport and Optical Properties of Inhomogeneous Media, J. C. Garland and D. B. Tanner, eds., AIP Conf. Proc. No. 40, Am. Inst. Phys., NY (1978).

53. A. Ignatiev, P. O'Neill, C. Doland and G. Zajac, Appl. Phys. Lett., 34 (1979), 42.

54. A. Ignatiev, P. O'Neill, G. Zajac and C. Boland, Proc. 2nd Annu. Conf. on Absorber Surfaces for Solar Receivers, Boulder, CO, Jan. 24, 1979, in Rep. SERI/TP-49-182, p. 9, Solar Energy Research Institute, Boulder, CO.

55. C. G. Granqvist and O. Hunderi, J. Appl. Phys., 50 (1979), 1058.

56. O. Hunderi and C. G. Granqvist, Thin Solid Films, 57 (1979), 303.

57. B. Window, I. T. Ritchie and K. Cathro, Thin Solid Films, 57 (1979), 309.

58. R. Clausius, Die mechanische Behandlung der Electricität, Vieweg, Braunschweig (1897), p. 62.

59. O. F. Mossotti, Memorie di Matematica e di Fisica della Societa Italiana della Scienze Residente in Modena, Vol. 24, pt. 2 (1850), 49.

60. C. G. Gillespie, ed., Dictionary of Scientific Biography, Vol. IX, Scribner's, NY (1974), p. 547.

61. C. J. F. Böttcher, Theory of Electric Polarisation, 1st Ed., Elsevier, Amsterdam (1952), p. 415.

62. R. W. Cohen, G. D. Mody, M. D. Coutts and B. Abeles, Phys. Rev., B8 (1973), 3689.

63. F. L. Galeener, Phys. Rev. Lett., 27 (1971), 421.

64. C. G. Granqvist, "Optical Properties of Ultrafine Gold Particles," in Electrical Transport and Optical Properties of Inhomogeneous Media, J. C. Garland and D. B. Tanner, eds., AIP Conf. Proc. No. 40, Am. Inst. Phys., NY (1978).

65. H. A. Lorentz, The Theory of Electrons, B. G. Teubner, Leipzig (1909), reprinted Dover, NY (1952).

66. W. L. Bragg and A. B. Pippard, Acta Cryst., 6 (1953), 865.

67. P. O'Neill and A. Ignatiev, Phys. Rev., B18 (1978), 6540.

68. D. E. Aspnes, Thin Solid Films, 89 (1982), 249.

69. O. Hunderi, Thin Solid Films, 57 (1979), 15.

70. G. B. Smith, Appl. Phys. Lett., 35 (1979), 668.

71. R. C. McPhedran and D. R. McKenzie, Proc. Royal Soc., A359 (1978), 45.

72. W. Lamb, D. M. Wood and N. W. Ashcroft, "Optical Properties of Small Particle Composites: Theories and Applications," in Electrical Transport and Optical Properties of Inhomogeneous Media, J. C. Garland and D. B. Tanner, eds., AIP Conf. Proc. No. 40, Am. Inst. Phys., NY (1978).

73. D. R. McKenzie, R. C. McPhedran and G. H. Derrick, Proc. Royal Soc., A362 (1978).

74. R. Fuchs, Phys. Rev., B11 (1975), 1732.

75. P. B. Johnson and R. W. Christy, Phys. Rev., B9 (1974), 5056.

76. A. S. Barker, Jr. and J. A. Ditzenberger, Phys. Rev., B1 (1970), 4358.

77. A. S. Siddiqui and D. M. Treherne, Infrared Phys., 17 (1977), 33.

78. D. R. Renneke and D. W. Lynch, Phys. Rev., 138 (1965), A530.

79. G. Lucovsky, R. J. Sladek and J. W. Allen, Phys. Rev., B16 (1977), 4716.

80. R. I. Frank and W. L. Moberg, J. Vac. Sci. Technol., 4 (1967), 133.

81. G. B. Smith and A. Ignatiev, Solar Energy Mater., 2 (1980), 461.

82. R. B. Pettit, R. R. Sowell and I. J. Hall, "Black Chrome Solar Slective Coatings Optimized to High Temperature Applications," Solar Energy Mater. (submitted).

83. O. S. Heavens, Optical Properties of Thin Solid Films, Dover, NY (1965), 63-79.

84. I. Webman, J. Jortner and M. H. Cohen, Phys. Rev., B15 (1977), 5712.

85. J. Spitz, T. Van Dahn and A. Aubert, Solar Energy Mater., 1 (1979), 189.

86. C. M. Lampert and J. Washburn, Solar Energy Mater., 1 (1979), 81.

87. G. S. son Frey, Z. Electrochem., 38 (1932), 260.

88. Van de Hulst, Light Scattering by Small Particles, John Wiley, NY (1957).

89. P. H. Holloway in Scanning Electron Microscopy, Vol. 1, SEM, Inc. (1978), 361-374.

90. P. H. Holloway, Surf. Sci., 66 (1977), 479.

91. P. J. Call, National Program Plan for Absorber Surface R & D, Rep. SERI/TR-31-103, 1979, Solar Energy Research Institute, Boulder, CO.

92. R. B. Pettit and R. R. Sowell, "Black Chrome Solar Selective Coating," Proc. Line Focus Conf., Sept. 9-11, 1980, Albuquerque, NM.

93. R. R. Sowell, private communication.

94. W. J. Diamond, Practical Experiment Design, Lifetime Learning Publ., Belmont, CA (1981).

95. Labsphere, P.O. Box 70, North Road, North Sutton, NJ 03260.

96. R. B. Pettit and A. R. Mahoney, "Portable Instrumentation for Solar Absorptance and Emittance Measurements," Proc. Line-Focus Conf., Sept. 9-11, 1980, Albuquerque, NM.

97. R. B. Pettit and R. R. Sowell, J. Eng. Power, 100 (1978), 489.

98. Oriel Corporation, P.O. Box 1395, 15 Market Street, Stamford, CT 06904.

99. AE Emissometer Instruction Manual, Devices and Services Company, 10911 Dennis Road, Suite 405, Dallas, TX 75229.

100. Standard Test Method for Solar Absorptance, Reflectance and Transmittance of Materials Using Integrating Spheres. This proposed practice of ASTM Committee E44 (draft #136R4) is a draft under development.

101. Standard Direct Normal Solar Spectral Irradiance at Air Mass 1.5. This proposed practice of ASTM Committee E44 (Committee Document #105) is a draft under development.

102. Standard Extraterrestrial Solar Irradiance Distribution, E490-73A, Annual Book of ASTM Standards, No. 41.

103. P. H. Holloway and G. E. McGuire, Thin Solid Films, 53 (1978), 3.

104. A. W. Czanderna, eds., Methods and Phenomena, Their Applications in Science and Technology, Vol. 1. Methods of Surface Analysis, Elsevier, Amsterdam (1975).

105. J. I. Goldstein and H. Yakowitz, eds., Practical Scanning Electron Microscopy, Plenum, NY (1977).

106. H. Hopster and C. R. Brundle, J. Vac. Sci. Technol., 16 (1979), 548.

107. P. S. Ho, J. E. Lewis, H. S. Wildman and J. K. Howard, Surf. Sci., 57 (1976), 393.

108. D. J. Young and M. Cohen, J. Electrochem. Soc., 124(5) (May, 1977), 769.

109. E. I. Alessandrini and V. Brusic, J. Vac. Sci. Technol., 9(1) (1972), 83.

110. G. A. Hope and I. M. Ritchie, Thin Solid Films, 34 (1976), 111.

111. S. Ekelund and G. Leygraf, Surf. Sci., 40 (1973), 197.

112. O. Kubaschewski and B. E. Hopkins, Oxidation of Metals and Alloys, Butterworths, London (1962).

113. D. Kaplan, A. Harvey and M. Cohen, Corr. Sci., 3 (1963), 161.

114. W. C. Hazel and A. U. Seybolt, J. Electrochem. Soc., 108(12) (Dec., 1961), 1146.

115. P. Kofstad, High Temperature Oxidation of Metals, J. Wiley and Sons (1966)

116. K. P. Lillerud and P. Kofstad, J. Electrochem. Soc., 127(11) (Nov., 1980), 2397.

117. K. P. Lillerud and P. Kofstad, J. Electrochem. Soc., 127(11) (Nov., 1980), 2410

118. P. H. Holloway and E. B. Evans, Oxid. Met., 4 (1972), 27

119. Available from Statistical Analysis Systems Institute, Inc., SAS Circle, Box 8000, Cary, NC 27511.

120. P. E. Green, Analyzing Multivariate Data, Dryden, Hinsdale, IL (1978)

121. W. Mendenhall and R. L. Schaeffer, Mathematical Statistics with Applications, Duxbury, North Scituate, MA (1973).

122. F. P. Fehlner and N. F. Mott, Oxid. Met., 2(1) (1970), 59

123. U. R. Evans, The Corrosion and Oxidation of Metals, Edward Arnold, Ltd., London (1960).

124. F. N. Rhines and R. G. Connell, Jr., J. Electrochem. Soc., 124(7) (June, 1977), 1122.

125. D. J. Young and M. Cohen, J. Electrochem. Soc., 124(5) (1977), 775

126. G. B. Smith, P. Hillery and K. Teytz, "Ranking Solar Absorber Structural Parameters in Terms of Impact on Performance and Stability," presented at the Intl. Conf. on Coatings, April 18-22, 1983, San Diego, CA

127. Metals Handbook, Vol. 2: Heat Treating, Cleaning and Finishing, Am. Soc. Metals, Metals Park, OH.

128. R. B. Pettit and C. J. Brinker, "Sol-Gel Protective Coatings for Black Chrome Solar Selective Films," presented at the SPIE Meeting, Jan. 28 and 29, 1982, Los Angeles, CA.

129. D. Polder and J. H. van Santen, Physica (Utr.), 12 (1946), 257.

130. G. B. Smith, J. Phys., 010 (1977), L39

131. S. L. Erickson, "Analytical Methods for the Control of Chromonyx Black Chrome Plating Baths," Sandia Rep. SAND 82-0467, 1982, Sandia National Laboratories

132. R. W. Atkins, *Physical Chemistry*, W. H. Freeman, San Francisco (1978)

133. P. H. Holloway, Surf. Sci., *54* (1976), 506

BIOGRAPHICAL SKETCH

Kartik Shanker was born in Madras, India, on December 18, 1951. After completing his high school education in New Delhi, he obtained his Bachelor of Technology degree in metallurgy in 1973 from the Indian Institute of Technology, Madras, India. Subsequently, he joined the University of Denver, Denver, Colorado, and obtained his Master of Science in 1975. His research was on superalloys. He joined the Department of Materials Science and Engineering at the University of Florida in 1979 and is pursuing the degree of Doctor of Philosophy. He is married and his wife, Latha, is currently a doctoral candidate in the Department of Finance, University of Florida.

Kartik has worked at the Defence Metallurgical Research Laboratory, Hyderabad, India (1976-77) and Forbes, Forbes, Campbell and Company, Ltd., Bombay (1977-79). His work experience encompasses electroslag refining, extrusion casting of aluminum alloys and cutting tool steels.

He is a student member of the American Vacuum Society and the International Society for Hybrid Microelectronics.

I certify that I have read this study and that in my opinion it conforms to acceptable standards of scholarly presentation and is fully adequate, in scope and quality, as a dissertation for the degree of Doctor of Philosophy.

Paul H Holloway

Dr. Paul H. Holloway, Chairman
Professor of Materials Science
and Engineering

I certify that I have read this study and that in my opinion it conforms to acceptable standards of scholarly presentation and is fully adequate, in scope and quality, as a dissertation for the degree of Doctor of Philosophy.

Dr. J. R. Ambrose
Associate Professor of Materials
Science and Engineering

I certify that I have read this study and that in my opinion it conforms to acceptable standards of scholarly presentation and is fully adequate, in scope and quality, as a dissertation for the degree of Doctor of Philosophy.

Chris Batich

Dr. C. D. Batich
Associate Professor of Materials
Science and Engineering

I certify that I have read this study and that in my opinion it conforms to acceptable standards of scholarly presentation and is fully adequate, in scope and quality, as a dissertation for the degree of Doctor of Philosophy.

Dr. S. S. Li
Professor of Electrical Engineering

This dissertation was submitted to the Graduate Faculty of the College of Engineering and to the Graduate School, and was accepted as partial fulfillment of the requirements for the degree of Doctor of Philosophy.

December, 1983

Wayne H Chen

Dean, College of Engineering

Dean for Graduate Studies
and Research